GROUND STATE, OPTICAL EXCITED STATES AND PHOTOINDUCED PHASE TRANSITION IN MIXED-STACK CHARGE TRANSFER COMPOUND TTF-CA

Ping Huai

September 29, 2000

Department of Synchrotron Radiation Science
School of Mathematical and Physical Science
The Graduate University for Advanced Studies

This doctor thesis is quoted from the following papers:

1. "Theory for Photoinduced Structural Phase Transition" P. Huai, H. Mizouchi and K. Nasu, Solid State Physics **34** (1999) 957 (in Japanese).

2. "Nonlinear Nonequilibrium Quantum Dynamics of Photoinduced Structural Phase Transitions" K. Nasu, H. Mizouchi and P. Huai, J. Luminescence **87-89** (2000) 86.

3. "Theory for Photoinduced Structural Phase Transitions and their Precursor Phenomena " H. Mizouchi, P. Huai and K. Nasu, Special Volume of [Phase Transitions], (Gordon and Breach, 2000) ed. by K. Nasu, in press.

4. "Theory for Photoinduced Structural Phase Transitions" H. Mizouchi, P. Huai and K. Nasu, Proceeding of LLDK2, July 24-26 2000, Tsukuba, Japan, to be published from AIP.

5. "Theory for Photoinduced Ionic-Neutral Structural Phase Transition in Quasi One-Dimensional Organic Molecular Crystal TTF-CA" P. Huai, H. Zheng and K. Nasu, J. Phys. Soc. Jpn **69** (2000) 1788.

6. "Theory of Photoinduced Phase Transition in the Quasi-One-Dimensional Charge Transfer Compound TTF-CA" P. Huai and K. Nasu, 2000 International Conference on Excitonic Processes in Condensed Matter (EXCON2000), Osaka, Japan.

7. "Variational Treatment of the Dynamical Pseudo Jahn-Teller System" P. Huai and H. Zheng, Phys. Lett. A **240** (1998) 341.

Oral Presentation:

"Theory of Photoinduced Phase Transition in the Quasi-One-Dimensional Charge Transfer Compound TTF-CA" 2000 International Conference on

Excitonic Processes in Condensed Matter (EXCON2000), August 22-25, 2000, Osaka, Japan.

Contents

Chapter 1

Introduction

As it is well known, solids are traditionally classified as metals, semiconductors and insulators. This classification provides us a useful general framework for material science both experimentally and theoretically. If we focus on organic molecular crystals, they are also typically classified into insulators, semiconductors, conductors or even superconductors. Among these various organic materials, in the present study, we will be concerned with a specific class of organic solids, in which two kinds of molecules, called donor (D) and acceptor (A), are stacked by 1 to 1 composition ratio. In these materials, D and A molecules often stack alternately along one of crystal axes, forming vast number of chains, and the interactions between these chains are usually quite weak. Therefore, such chain crystals are often theoretically treated as quasi one-dimensional (1-d) systems.

If we see much more in detail, they are also classified into two groups according to the way of stacking, as shown in Fig. 1.1. One is the segregated-stack where donor molecules and acceptor ones form their own respective chains. The other is the mixed-stack where donor and acceptor molecules are stacked alternately to form a single chain. In the later type of crystals, a charge transfer (CT) from D to A usually occurs yielding cations D^+ and anions A^-. Because the overlap between D

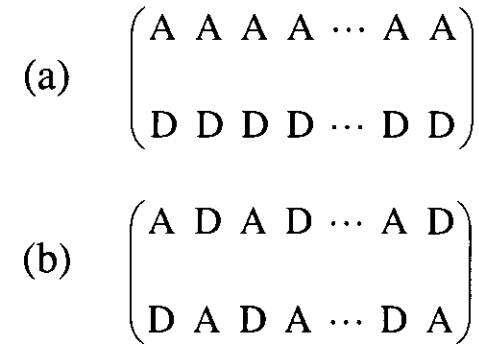

Fig. 1.1: Schematic picture of 1-d 1:1 molecular crystals. (a) Segregated-stack, (b) Mixed-stack.

and A hybridizes neutral states ($\cdots$ DA $\cdots$) with ionic ones ($\cdots$ D^+A^- $\cdots$), the charge transfer (ρ) from D to A always becomes fractional. Thus, the mixed-stack charge transfer crystals can be further classified into two groups according to this degree of the charge transfer ρ, the quasi neutral (N) phase with $\rho < 0.5$, and the quasi ionic (I) phase with $\rho > 0.5$.

Torrance *et al.* had studied a large number of mixed-stack charge transfer crystals.[1] It was shown that, at room temperature, some crystals are situated close to, and some far from the N-I boundary. For the neutral crystals near this boundary, by applying hydrostatic pressure or lowering the temperature, we can change their color distinctly. This reversible change of the color was interpreted as a phase transition from N phase to I one. A typical example for these materials is tetrathiafulvalene(TTF)-p-chloranil(CA). Since its discovery, this TTF-CA had been extensively studied in the past two decades for its unique optical and magnetic properties.[2]~[20]

In the early studies, the N-I phase transition in TTF-CA was discovered at a broad temperature region of about 30K width around $T_c = 84$K.[2] Thus, due to this result, it was regarded not to be a first order phase transition. However, this conclusion was soon refined by more exact experiments. The visible, infrared

reflectivity and ESR spectra in single crystals now indicate that it is a sharp first order transition at 84K. [3, 4, 5] The broadening of spectra in the original studies was ascribed to the bad quality of samples, like finite crystal size effects or residual impurities.

The low temperature I-phase is characterized by a lattice dimerization along the stacking direction, while the starting N-phase is monomeric and has no dimerization. Thus, this dimerization is a symmetry breaking order parameter, and describes the crystalline structure (electronic, position of nucleus,...) together with the charge transfer ρ.

The study by Jacobsen and Torrance[6] indicates that the light absorption spectral shape in the I-phase has a two-headed structure peaked at 0.6 eV and 1.0 eV. Because the optical dipoles of these two peaks are strongly polarized parallel to the stacking axis, they are ascribed to the CT excitations between TTF and CA molecules. According to the temperature resolved measurement from 300 K to 45 K, this peculiar two-headed shape appears only below T_c, while, above T_c, we have only a single peak at 0.6 eV.

Recently, the photoinduced I→N phase transition(PIPT) has been investigated by means of time-resolved spectroscopic techniques.[7, 8, 9] It was found that a macroscopic neutral domain can be generated in the I-phase of TTF-CA by shining a strong laser light of about 0.6 eV $\sim$ 2.2 eV onto it, even when the temperature is very low.

A number of theoretical studies have also been devoted to clarify this N-I phase transition.[21]~[40] The first model, which includes the effect of a finite itineracy of valence electrons, was studied by Soos and Mazumdar.[21] They found a discontinuous transition due to the Coulomb interaction within a mean-field approximation. Nagaosa studied the 1-d modified Hubbard model with inter-molecular Coulomb interaction by the quantum Monte-Carlo simulation.[22, 23, 24, 25] Investigating the

lattice-relaxed excited states, he clarified the neutral-ionic domain wall (NIDW), as well as various other soliton structures.[25] Sakano and Toyozawa have studied the ground state properties of TTF-CA, using a long range Coulomb interaction model.[26] They also showed the origin of the double-peak structure in the optical absorption spectra of the I-phase. The possibility of dimerized mixed-stack charge transfer crystals and the existence of soliton-like excitations have also been studied by using various other methods, ranging from the valence-bond technique for finite rings,[27]~[31] the real-space renormalization group theory,[32] to numerous other theoretical methods[33]~[40].

In the present work, we will investigate the nonlinear lattice relaxation of the charge transfer exciton, to shed light on the mechanism of the aforementioned photoinduced I→N phase transition, as well as the ground state properties and the absorption spectral shape of TTF-CA, from a unified point of view. Within the adiabatic approximation and the mean-field theory, an extended Peierls-Hubbard model will be studied to clarify those properties.

The remaining parts of this work are organized as follows. In Chapter 2, the experimental and theoretical studies will be reviewed for the structural and optical properties of TTF-CA. Chapter 3 is devoted to the mean-field treatment and the perturbation calculations for the extended Peierls-Hubbard model. In Chapter 4, we present our theoretical results for the properties of TTF-CA in the ground state. In Chapter 5, we give the numerical results for the optical excited states and the absorption spectra. The analysis of the nonlinear lattice relaxation of the exciton will be demonstrated with the numerical results in Chapter 6. Future prospect will be presented in Chapter 7. In the final chapter, we will sum up the work and give the conclusion.

Chapter 2

General Properties of TTF-CA

2.1 N-I Boundary of Mixed-Stack Charge Transfer Crystal

In contrast to inorganic compounds, the overlap (transfer energy) between neighboring molecules in an organic solid is rather small compared with other energies involved, and, in a rough approximation, it can be neglected. A simple theory had been applied to the mixed-stack charge transfer compound by McConnell.[41] In his theory, two energies are considered. One is the cost of ionizing a donor-acceptor (D-A) pair, which is denoted as $(I - A)$. I is the ionization potential of the donor and A is the acceptor electron affinity. The other is the electrostatic Madelung energy, which is denoted as $\alpha\langle\frac{e^2}{a}\rangle$ (α : Madelung constant). The total energy per D-A pair is then given by

$$E(\rho) = (I - A)\rho - \alpha\langle\frac{e^2}{a}\rangle\rho^2 \ , \tag{2.1}$$

where ρ is the degree of charge transfer. For $0 \leq \rho \leq 1$, the lowest value of the energy $E(\rho)$ occurs for one of the two possible values of ρ: (1)$\rho = 0$ if $I - A > \alpha\langle\frac{e^2}{a}\rangle$, and this solid is neutral; or (2) $\rho = 1$ if $I - A < \alpha\langle\frac{e^2}{a}\rangle$, and this solid is ionic. In the

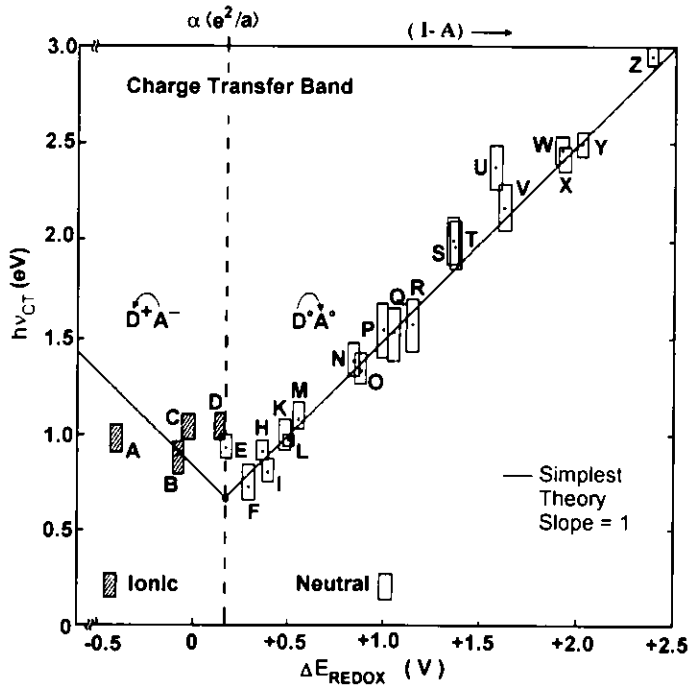

Fig. 2.1: Comparison of simplest model with $h\nu_{\rm CT}$ for the compounds in Table (2.1).[1]

neutral solid, the lowest energy excitation corresponds to the transfer of an electron from a donor to a neighboring acceptor along the stacking axis. The energy of this charge-transfer transition is

$$h\nu_{\rm CT}^{\rm N} = (I - A) - \langle \frac{e^2}{a} \rangle \ . \tag{2.2}$$

For an ionic solid, the lowest excitation corresponds to the transfer of an electron from a charged acceptor back onto a neighboring donor:

$$h\nu_{\rm CT}^{\rm I} = (2\alpha - 1)\langle \frac{e^2}{a} \rangle - (I - A) \ . \tag{2.3}$$

These calculated values of $h\nu_{\rm CT}$ are plotted as the V-shaped straight lines in Fig. 2.1 versus (I-A). The vertical dashed line is the neutral-ionic boundary, where $I - A = \alpha\langle \frac{e^2}{a} \rangle$.

Torrance suggested that the pressure would decrease the spacing between molecules, increase the Madelung energy, and hence shift the boundary in Fig. 2.1 towards the

symbol	Compound	N/I
A	TMPD-tetrafluoroTCNQ	I
B	dimethylphenazine-TCNQ	I
C	TMPD-TCNQ	I
D	TMPD-chloranil	I
E	TMDAP-TCNQ	N
F	TTF-chloranil	N
G	TTF-fluoranil	N
H	DibenzeneTTF-TCNQ	N
I	DEDMTSeF-diethylTCNQ	N
J	TMDAP-fluoranil	N
K	TTF-dichlorobenzoquinone	N
L	perylene-tetrafluoroTCNQ	N
M	perylene-DDQ	N
N	perylene-TCNE	N
O	perylene-TCNQ	N
P	TTF-dinitrobenzene	N
Q	perylene-chloranil	N
R	pyrene-TCNE	N
S	pyrene-chloranil	N
T	anthracene-TCNE	N
U	hexamethylbenezene-chloranil	N
V	naphthalene-TCNE	N
X	anthracene-PMDA	N
Y	anthracene-tetracyanobenzene	N
Z	phenanthrene-PMDA	N

Table 2.1: Name list of the compounds in Fig. 2.1.

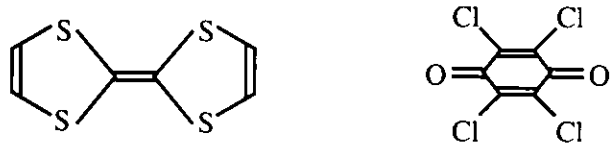

TTF CA

Fig. 2.2: Molecule TTF and CA.

right.[1] If the boundary shifts far enough, the neutral compound would become ionic. This is a simple explanation for the pressure induced N-I phase transition.

Torrance further suggested that the neutral compound closed to the N-I boundary might undergo the same transition at low temperature, presumably driven by the thermal contraction. In this case, it is temperature induced N-I phase transition.

TTF-CA is a typical mixed-stack CT compound among those close to the N-I boundary. It was studied extensively on its electric, magnetic, optical and thermodynamical properties, since its discovery.

2.2 Crystal Structure

The organic π-electron donor TTF and the acceptor CA are both planar molecules. Their molecular structures are shown in Fig. 2.2.

The 3-dimensional crystal structure of TTF-CA is shown in Fig. 2.3. The monoclinic unit-cell contains two TTF-CA units. In the N-phase, the space group is $P12_1/n1$ and the unit cell contains two equivalent nondimerized stacks. Figure 2.4 illustrates the schematic drawing of its structural change from N- to I-phase. There is no alteration of the multiplicity of the unit cell, and the symmetry lowering is characterized by dimerization. Hence, I-phase space group is P1n1 with a ferroelectric arrangement of two equivalent dimerized stacks related by the glide plane.

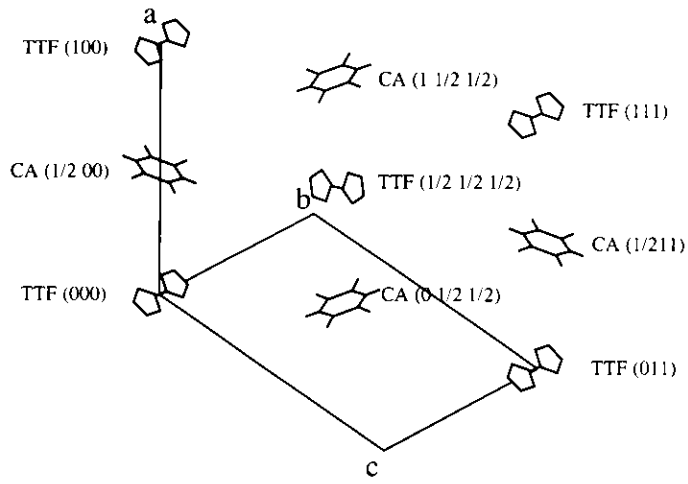

Fig. 2.3: The 3-dimensional structure of TTF-CA crystal.

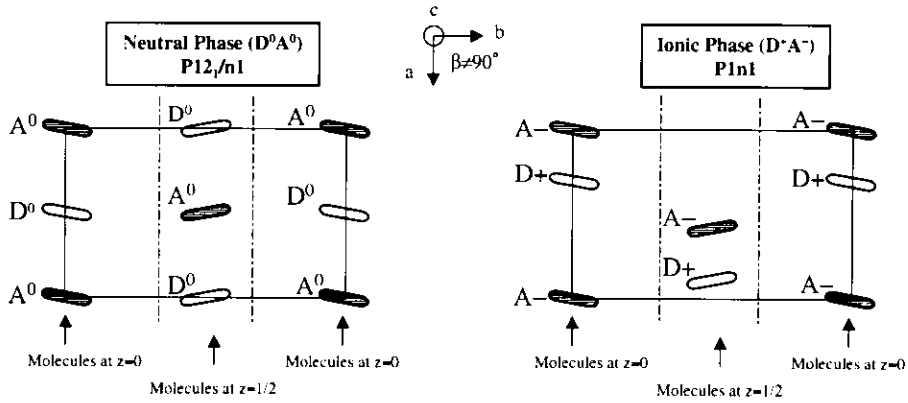

Fig. 2.4: Schematic drawing of the TTF-CA structure in the N-phase and its modification in the I-phase.

In the following three sections, three types of N-I phase transitions (the temperature induced, the pressure induced and the photoinduced ones) will be shown with a variety of experimental results in close connection with our present work. These results provide us with very important information about the microscopic structure of TTF-CA crystal and their variations under different physical environments. The phenomenological theory presented in this work depends closely on this information, and we try to give a unified picture to clarify these properties, especially focusing on the photoinduced phase transition.

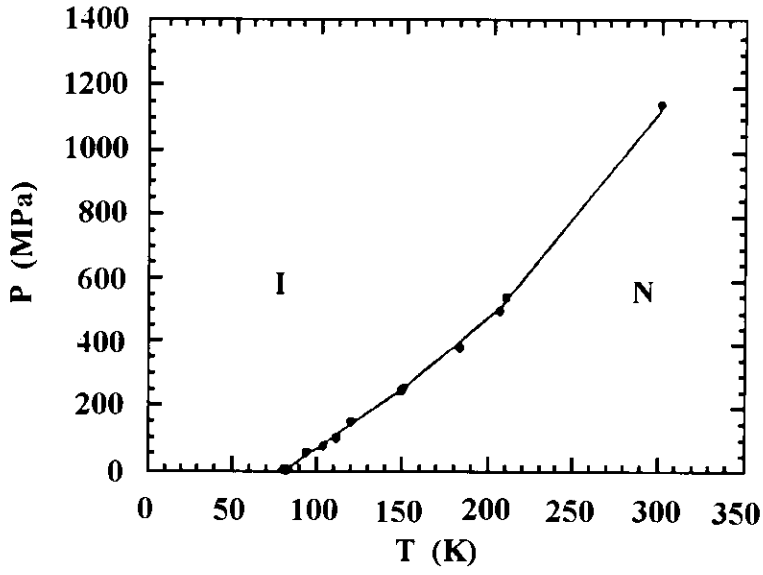

Fig. 2.5: Phase diagram of the N-I transition of TTF-CA. [46]

2.3 Temperature Induced N-I Phase Transition

As we have already mentioned, N-I phase transition can be obtained not only by lowering the temperature but also by increasing the pressure, as shown in the phase diagram Fig. 2.5. In this section, the temperature induced N-I phase transition is surveyed by keeping samples at atmospheric pressure, if it is not specified.

The symmetry breaking and the structural change are the most essential points in the studies of N-I phase transition. The crystal structure of TTF-CA was first investigated by using X-ray diffraction analysis at room temperature. [10] Its space group is, as already mentioned, $P12_1/n1$, and the unit cell contains two equivalent nondimerized stacks with alternation of TTF and CA molecules located on inversion centers $(\frac{1}{2}\frac{1}{2}0)$ and $(0\frac{1}{2}0)$. Because neutron diffraction has the advantage to yield more reliable information on light elements than X-ray diffraction, it is a suitable tool to analyze the intramolecular and intermolecular changes with respect to dimerization process in the N-I phase transition.

Cointe *et al.* had undertaken a direct and complete investigation of the structural

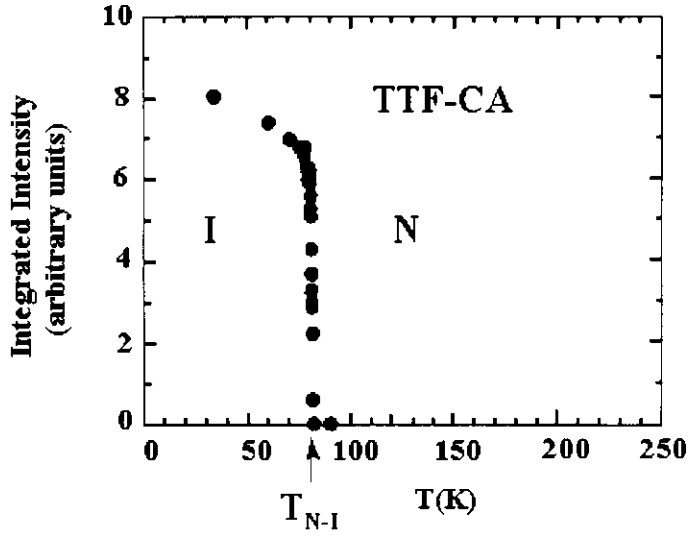

Fig. 2.6: Evolution with temperature of the integrated intensity of the characteristic reflection (030). Error bars are smaller than the diameter of the symbols indicating the good quality of the data.[11]

aspects associated with the N-I phase transition in TTF-CA by neutron scattering techniques.[11] According to their results, N-phase has two types of systematic extinctions due to the monoclinic symmetry $P12_1/n1$. One is $0k0 : k =$ **odd number** because of the screw axis 2_1 parallel to b. The other is $h0l : h + l =$ **odd number** because of the glide plane n parallel to (**a**,**c**). On the other hand, only the $0k0 : k =$ **odd number** reflections appear below the transition temperature T_{N-I} with a significant intensity as shown in Fig. 2.6, while the $h0l : h + l =$ **odd number** reflections remain systematically absent in the ionic phase. These features imply the lack of the two-fold screw axis 2_1 but the persistence of the glide plane n in the low temperature phase. Thus, the space group of the I-phase is $P1n1$ with a ferroelectric arrangement of two equivalent dimerized stacks and a dipole moment lying the (**a**, **c**) plane.

Besides the symmetry breaking, the cell parameters shown in Fig. 2.7, 2.8 and 2.9 also give some structural evidence of the phase transition. On one hand, the

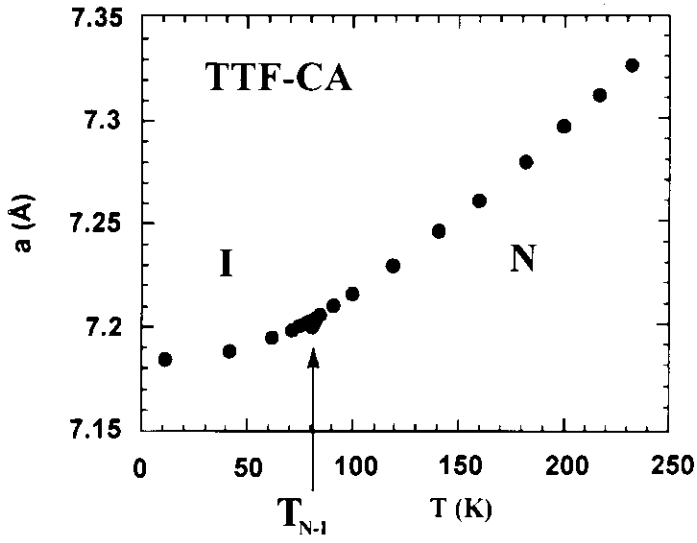

Fig. 2.7: Evolution with temperature of the cell parameter **a**. [11]

contraction of the stacking axis **a** with decreasing temperature is shown in Fig. 2.7. The phase transition temperature is indicated by a simple change of the slope, as the contraction is noticeably reduced in the I-phase. On the other hand, the **b** and **c** cell parameters present an abrupt jump at T_c(T_{N-I}), which is much more pronounced for $\Delta \mathbf{b}/\mathbf{b} \cong 0.5\%$ than for $\Delta \mathbf{c}/\mathbf{c} \cong 0.1\%$. This behavior strongly evidences the three-dimensional nature of the interaction.

The positions of all the atoms in the unit cell of TTF-CA have been determined by using the neutron diffraction technique for N- and I-phases, as shown in Table 2.2.

According to these neutron diffraction data, the structural deformations in the I-phase mainly take place in the dimerization along the stacking axis **a**, as shown by Table (2.3). Two distinct D-A distances, $d_{\text{intra}} = 3.504$Å and $d_{\text{inter}} = 3.685$Å alternate along the stacking direction, compared to the single D-A distance $d = 3.70(1)$Å in the N-phase. The dipole moment is calculated approximately by assuming the partial charge ($\rho \cong 0.7$) transferred from D to A in the I-phase.

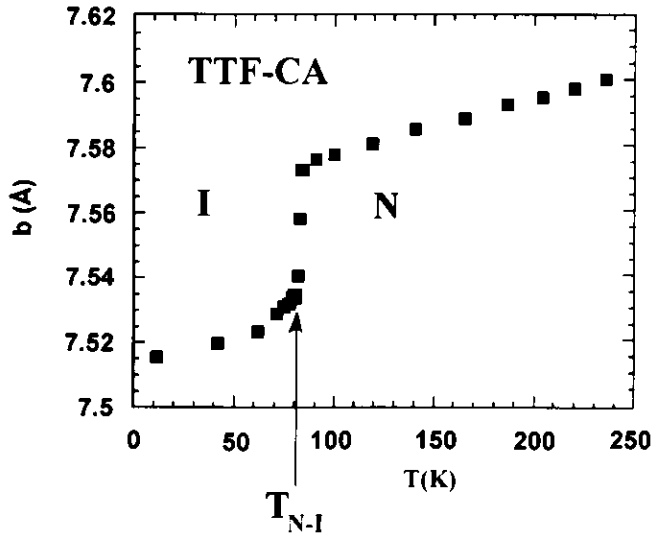

Fig. 2.8: Evolution with temperature of the cell parameter **b**. [11]

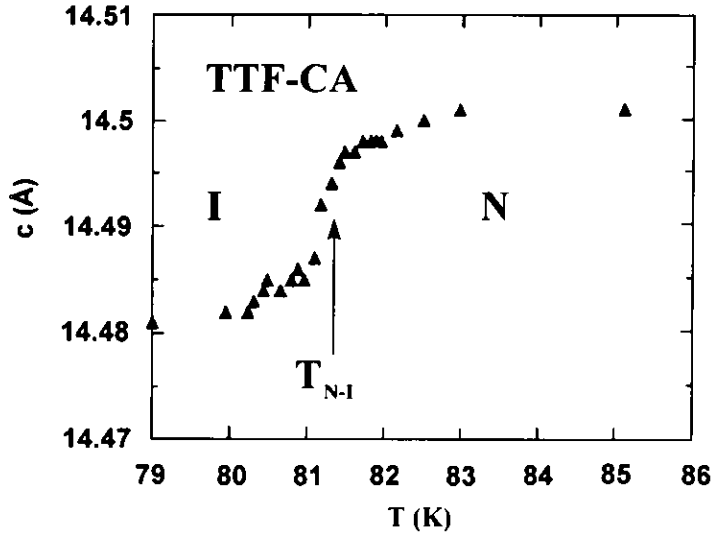

Fig. 2.9: Evolution with temperature of the cell parameter **c**. [11]

Atom	x/a	y/b	z/c	Atom	x/a	y/b	z/c
	T = 300 K				T = 90 K		
C1	3131(2)	1465(2)	-940(1)	C1	3097(2)	1418(2)	-933(1)
C2	4627(2)	4338(2)	-283(1)	C2	4621(2)	4327(1)	-284(1)
C3	3369(2)	2409(2)	-1680(1)	C3	3356(2)	2361(2)	-1685(1)
S4	3866(5)	2379(5)	142(2)	S4	3857(4)	2365(4)	164(2)
S5	4394(5)	4450(6)	-1494(2)	S5	4425(4)	4417(4)	-1502(2)
H6	2499(6)	161(5)	-952(3)	H6	2463(5)	128(4)	-950(2)
H7	2985(6)	1992(6)	-2400(3)	H7	2978(5)	1948(4)	-2405(2)
C15	407(2)	6400(2)	-614(1)	C15	445(2)	6391(2)	-626(1)
C16	-448(2)	4730(2)	-986(1)	C16	-436(2)	4716(2)	-989(1)
C17	-788(2)	3416(2)	-414(1)	C17	-800(2)	3401(2)	-407(1)
O18	824(3)	7540(3)	-1123(1)	O18	899(2)	7523(2)	-1144(1)
C*l*19	-892(2)	4553(2)	-2161(1)	C*l*19	-870(1)	4500(1)	-2178(1)
C*l*20	-1661(2)	1457(2)	-822(1)	C*l*20	-1694(1)	1424(1)	-819(1)
				T = 40 K			
Atom	x/a	y/b	z/c	Atom	x/a	y/b	z/c
C1	3099	1418(1)	-938	C8	6909(1)	8603(1)	936(1)
C2	4497(1)	4368(1)	-281(1)	C9	5259(1)	5739(1)	-298(1)
C3	3398(1)	2360(1)	-1674(1)	C10	6664(1)	7634(1)	1706(1)
S4	3751(3)	2395(3)	176(1)	S11	6090(3)	7658(3)	-135(1)
S5	4427(3)	4471(3)	-1496(1)	S12	5555(3)	5621(3)	1508(1)
H6	2436(3)	124(2)	-983(1)	H13	7563(3)	9933(3)	917(1)
H7	3113(2)	1971(2)	-2416(1)	H14	7105(3)	8067(3)	2416(2)
C15	642(1)	6373(1)	-591(1)	C21	-335(1)	3585(1)	674(1)
C16	-265(1)	4691(1)	-947(1)	C22	558(1)	5259(1)	1027(1)
C17	-673(1)	3393(1)	-364(1)	C23	948(1)	6581(1)	429(1)
O18	1125(1)	7500(1)	-1124(1)	O24	-819(1)	2432(1)	1196(1)
C*l*19	-796(1)	4517(1)	-2148(1)	C*l*25	883(1)	5549(1)	2211(1)
C*l*20	-1649(1)	1427(1)	-783(1)	C*l*26	1785(1)	8596(1)	855(1)

Table 2.2: The fractional atomic coordinates($\times 10^{-4}$) in the unit cell of TTF-CA are listed with standard deviations in parentheses. T = 300 K and T = 90 K are in the N-phase while T = 40 K is in the I-phase. [11] The 3-d view for these atoms is given in Fig. 2.10.

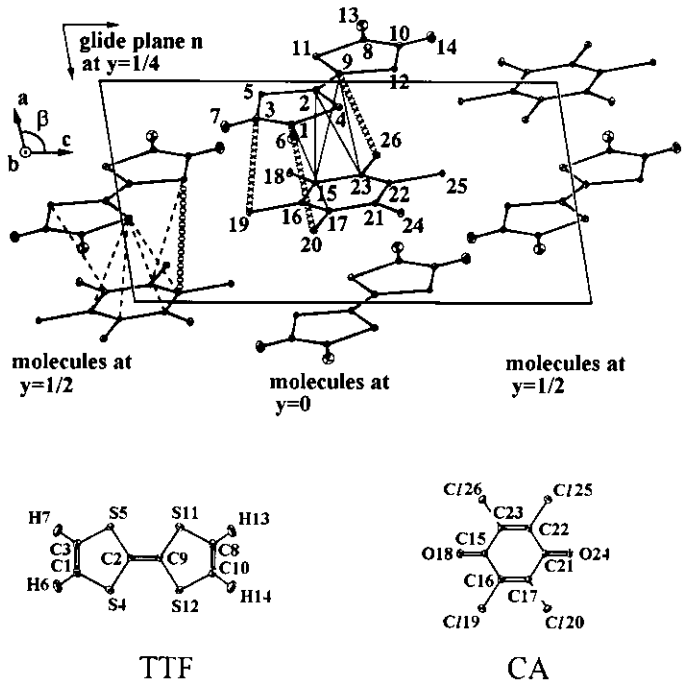

Fig. 2.10: The positions of constituent atoms in TTF-CA crystal. [11]

	a	b	c
Displacements (Å):			
TTF	-0.007(1)	0,019(1)	0.0035(6)
CA	0.0842(6)	-0.0061(6)	0.0523(3)
Dipole moment (Debye):			
In the chain	-0.30(6)	-0.09(3)	-0.15(3)
In the unit cell	-0.6(1)	0.00(6)	-0.30(6)

Table 2.3: Molecular center displacements (Å) at 40 K, compared to the neutral phase, and the corresponding dipole moment (Debye) along the crystallographic axes **a**, **b**, **c**. [11]

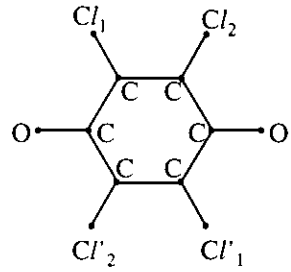

CA MOLECULE

Bond lengths (Å)	T=300K	T=90K	T=40K
C-Cl_1	1.700(3)	1.708(5)	1.724(1)
C-Cl'_1			1.705(1)
C-Cl_2	1.697(3)	1.704(4)	1.711(1)
C-Cl'_2			1.714(1)

Fig. 2.11: The chloranil (CA) molecule and C-C*l* bond lengths at different temperatures. Primed and unprimed atoms are symmetrically equivalent in the N-phase.[12]

Figure 2.11 displays the intra-molecular bond length of the CA molecules at different temperatures. Both charge-transfer increases and symmetry breaking at T_c contribute to the changes between the N- and the I-phases.

Since its discovery, the TTF-CA has also been studied by using various spectroscopic techniques sensitive to electronic states. Figure 2.12 shows the polarized reflection spectra of TTF-CA crystal of the (001) face at temperatures well below and above the transition temperature, for the electric vectors parallel and perpendicular to the stacking axis **a**. Those appearing in near infrared region $A_1 \sim A_3$ are due to the CT excitations, while the others B$\sim$F in the visible region are attributed to the intra-molecular transitions in TTF(B$\sim$E) and CA(F) molecules. The CT excitation bands are strongly polarized parallel to the stacking axis because of the 1-d overlap along the **a**-axis, while the intra-molecular excitation bands in TTF are predominantly polarized perpendicular to the **a** axis, as their transition dipoles lie

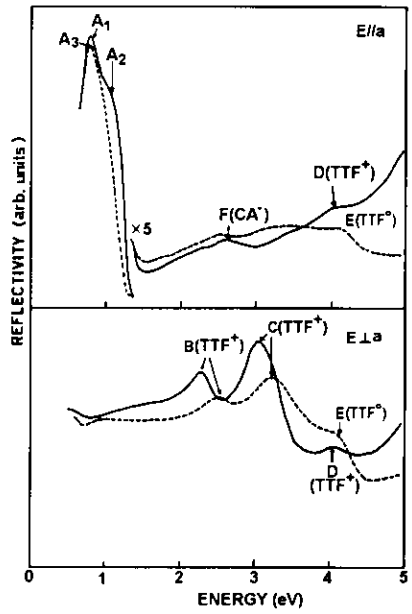

Fig. 2.12: Polarized reflection spectra of TTF-CA single crystal observed at 2K (solid lines) and at 290 K (broken lines) . [3]

on the TTF molecular plane.

There is a marked difference between the spectra in the I- and N-phases. In more detail, the spectra of the $A_1 \sim A_3$ bands and of the B$\sim$E bands are plotted at various temperature across T_c in Fig. 2.13. In the CT excitation band, a shoulder-like structure A_2 observed in the I-phase, suddenly disappears at around $T_c \cong 84$K. The change is even more drastic in the TTF intra-molecular transition bands. With increasing temperature, the B- and C- bands in the I-phase abruptly shift by about 0.2 eV toward high energy side at $T_c \cong 84$K.

The CT absorption spectra obtained by using Kramers-Kronig analysis of the reflectance are shown in Fig. 2.14. At room temperature, the CT absorption band peaks near 0.6 eV, while at low temperature, a second peak starts to appear at its high energy side, near 1.0 eV.

Electron spin resonance (ESR) is powerful tool to study the magnetic defects and their thermodynamics in the crystal. In Fig. 2.15, temperature-dependent ESR

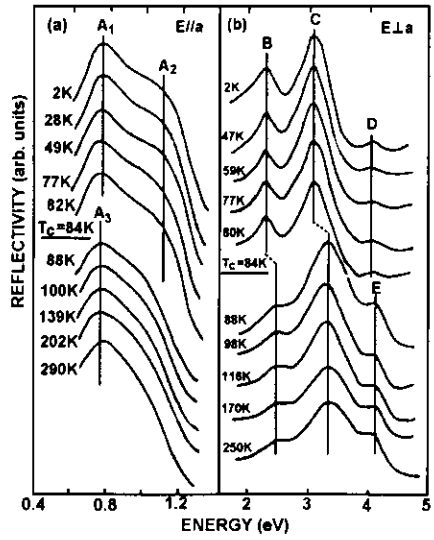

Fig. 2.13: Temperature changes of the charge-transfer excitation band (a) and of the intra-molecular excitation bands (b) across the neutral-ionic phase-transition temperature $T_c = 84K$. [3]

profile is demonstrated near T_c for TTF-CA single crystal. A week and narrow ESR signal observed slightly above T_c is significantly enhanced as the temperature is lowered across T_c, and then becomes considerably broadened below T_c. Meanwhile, the integrated intensity increases continuously with decreasing temperature. These lines fit with Lorentzian curves quite well through the whole temperature range, and that is naturally attributed to the motional-narrowing effect.

The total spin susceptibility is plotted in Fig. 2.16 against T^{-1}. The dc conductivity measured along the stacking axis is also shown for comparison. The susceptibility is negligibly small above T_c and shows a sharp discontinuous rise at T_c. In the ionic region below T_c, the total spin susceptibility follows a Curier law, indicating a constant spin density at $T < T_c$. Simultaneously, the dc conductivity shows a jump, indicating the creation of mobile charge carriers at the onset of the I-phase, although this crystal is still an insulator.

^{35}Cl nuclear quadrupole resonance (NQR) measurements performed on a TTF-

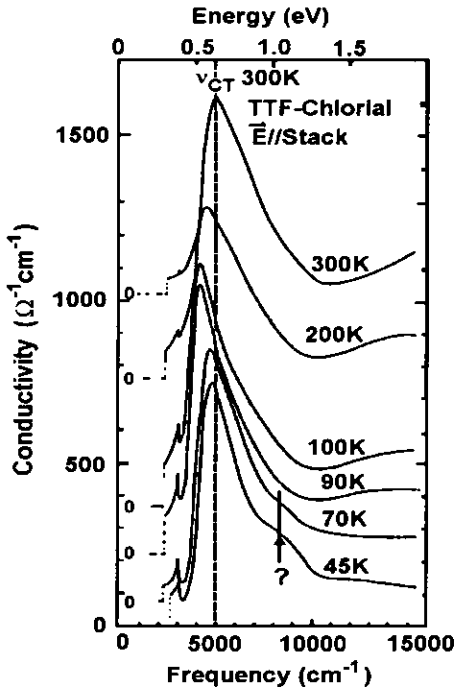

Fig. 2.14: The frequency dependent conductivities are obtained from a Kramers-Kronig analysis of the reflectance, showing the temperature dependence of the CT absorption peak. [6]

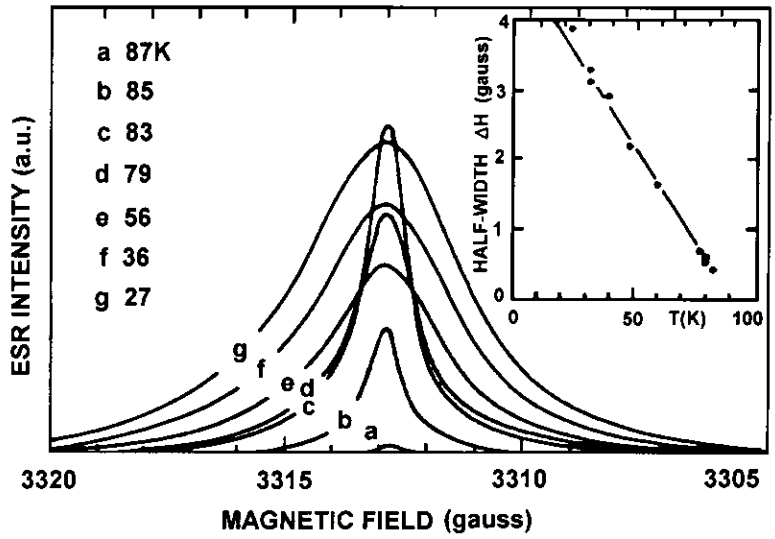

Fig. 2.15: The ESR line shapes and the half widths (inset) of TTF-p-CA single crystal near $T_c = 84K$. [5]

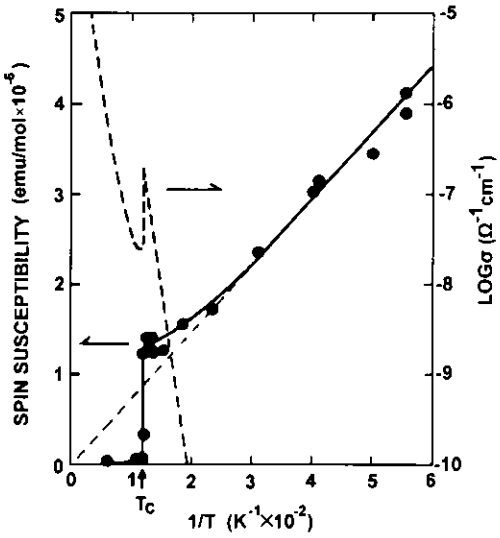

Fig. 2.16: The total spin susceptibility and dc electric conductivity (dashed curve) of TTF-CA single crystal plotted against T^{-1}. Dashed straight line represents the paramagnetic Curie law. [5]

CA single crystal are demonstrated in Fig. 2.17. In the N-phase ($T > T_c$), the TTF-CA ^{35}Cl NQR spectrum is composed of two resonance lines, a high frequency (HF) and a low frequency (LF) ones, at 37887 kHz and 37157 kHz for T=91 K, which correspond to the two kind of symmetry independent chlorine atoms, Cl_1 and Cl_2, situated on the same CA molecules, as already shown in Fig. 2.11. In the I-phase, the four chlorine atoms, Cl_1 Cl_2 Cl'_1 and Cl'_2, of one CA molecule become symmetrically unequivalent (centrosymmetry loss), while the two CA molecules in the unit-sell are still related by the n glide plane.

As for the pressure induced N-I phase transition, TTF-CA undergoes a gradual transformation from the N-phase to the I one in an intermediate region from 0 to about 10 kbar, in contrast with the temperature induced first-order one.[13, 14] Therefore, this phase transition had been classified into the second order one with coexistence of quasi-neutral and quasi-ionic phases.

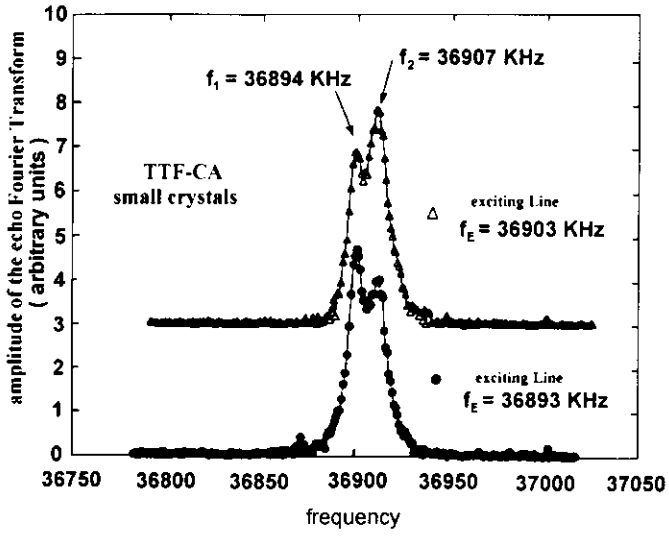

Fig. 2.17: NQR spectrum obtained from Fourier transform of echo signals in the I-phase at 77.4K. [12]

2.4 Photoinduced N-I Phase Transition

Based on femto-second laser pulse techniques, Koshihara *et al.* systematically studied the photoinduced N-I bi-directional phase transitions in TTF-CA.[7, 8] Comparing the time-resolved reflection spectra with the typical spectra in N- and I-phases, they demonstrated that the photoinjected localized excited states grow into macroscopic metastable domain, which could be as large as 200 $\sim$ 1000 neutral(ionic) pairs in the ionic(neutral) ground state.

The photoreflectance (PR) spectra in the N- and I-phases, are plotted in Fig. 2.18 (b,c). PR spectra were recorded as the relative difference between the spectra with and without irradiation by the pulse laser of 80-fs width. The photoirradiation was made at energies above the CT gap ($h\nu = 1.55$eV) and nearby the lower energy side of the localized intra-molecular excited state of TTF molecules.

Solid lines in (b) and (c) indicate the result well after pulsed excitation. It is noted that the shape of these PR spectra can be reproduced by the calculated differential spectra, $\{R(\mathrm{N}) - R(\mathrm{I})\}/R(\mathrm{I})$ and $\{R(\mathrm{I}) - R(\mathrm{N})\}/R(\mathrm{N})$. Here, $R(\mathrm{N})$ and $R(\mathrm{I})$ are the typical reflectance spectra in the N- and I-phases. This result clearly indicates that the photoexcitations of the crystal in the I- and N-phases cause macroscopic I-to-N and N-to-I phase conversions, respectively. A rough estimation shows that about 65% and 25% of the surface of the host I-phase and N-phase crystals were photoconverted into metastable N- and I-phases.

It should also be noted that, at 77 K, PR peaks observed around 3.0 eV well after excitation (Δt = 670 ps) seem to be located at higher photon energy sides immediately after excitation (Δt = 300 ps). This phenomenon indicate that there might appear a new domain entirely different from the neutral one, only in the early time of the photoexcitation.

The time profiles of the PR signals are plotted in Fig. 2.19 demonstrating the speed of the phase transition. The PR signals start to increase at Δt = 100 ps and

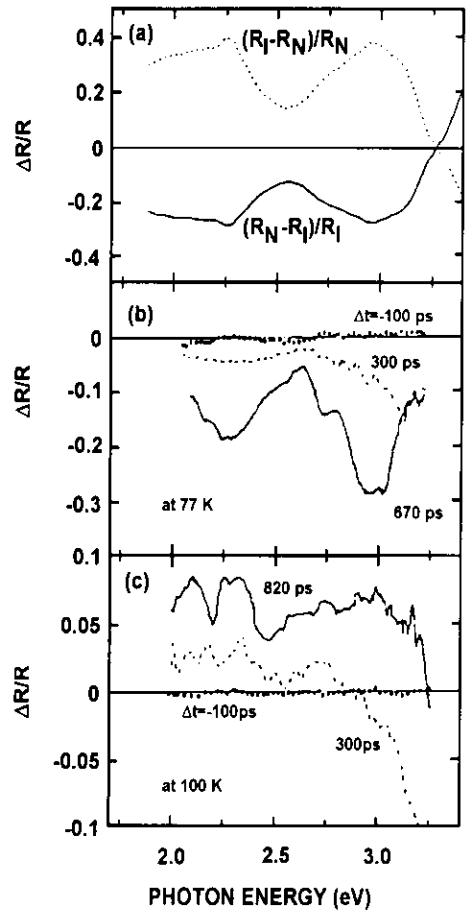

Fig. 2.18: (a)Calculated differential spectra $\{R(\mathrm{N}) - R(\mathrm{I})\}/R(\mathrm{I})$ and $\{R(\mathrm{I}) - R(\mathrm{N})\}/R(\mathrm{N})$ plotted by solid and dashed lines. Here, $R(\mathrm{N})$ and $R(\mathrm{N})$ are the typical reflectance spectra in the N- and I-phases. (b) and (c) Time-resolved photoreflectance(PR) spectra in the N- and I-phases, measured at 100 and 77K, respectively. [8]

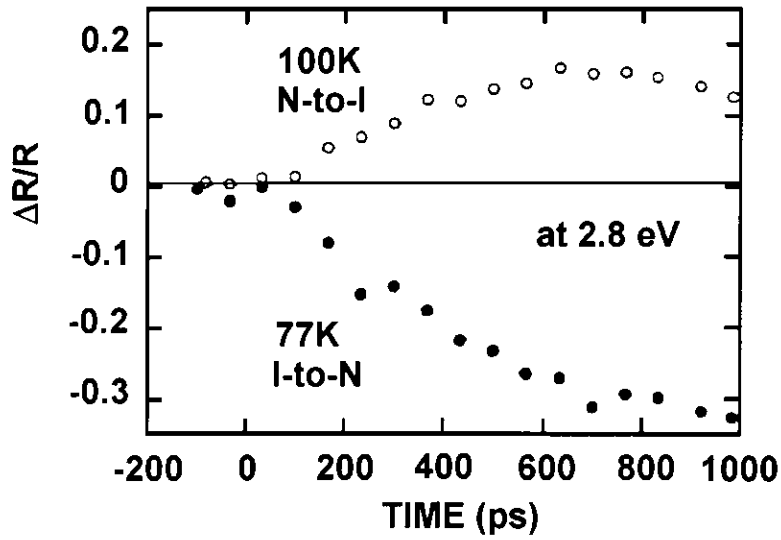

Fig. 2.19: Time profiles of the PR signals observed at 2.8 eV induced by the irradiation of 1.55-eV light pulse with 80-fs width. Results observed at 77 K (conversion form I-phase to N-phase) and 100 K 0(N-to-I conversion) are plotted by closed and open circles. The photon flux for excitation was 1×10^{14}cm^2. [8]

are gradually enhanced until they reach their optimum value at around $\Delta t = 700$ ps. These results indicate that local excited species, injected by an 80-fs laser pulse into the host I-phase (N-phase) crystal, grow into the macroscopic N-phase (I-phase) domain within a period of 1 ns.

The observed PR signals were transient and disappeared within 1 ms. That means the metastable phase domain can easily go back to the original stable one. According to analysis of a simple model, the height of the potential barrier between the stable and metastable phases is believed to be rather low at around T_c .

The dynamics of the N-I phase transition strongly depends on the excitation photon density. Figure 2.20 shows the time dependence of the PR signal observed with various excitation intensities. With rather week photoexcitation, the PR signal starts to increase 100 ps later after the irradiation of the light pulse. However, with higher intensity, the PR signal begins to increase immediately after excitation.

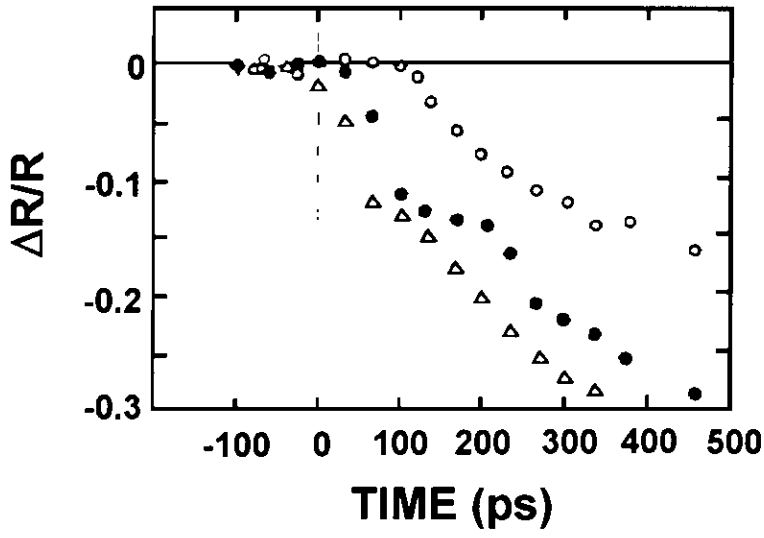

Fig. 2.20: Time dependence of the PR signal observed at 3.0 eV with various excitation intensities. Open circles, closed circles and triangles are for excitation intensities of 2×10^{18}, 9×10^{18} and $1.7 \times 10^{19}\mathrm{cm}^{-3}$, respectively. The sample temperature was 77K, and the crystal was in the I-phase before excitation by 1.55-eV light pulse. [8]

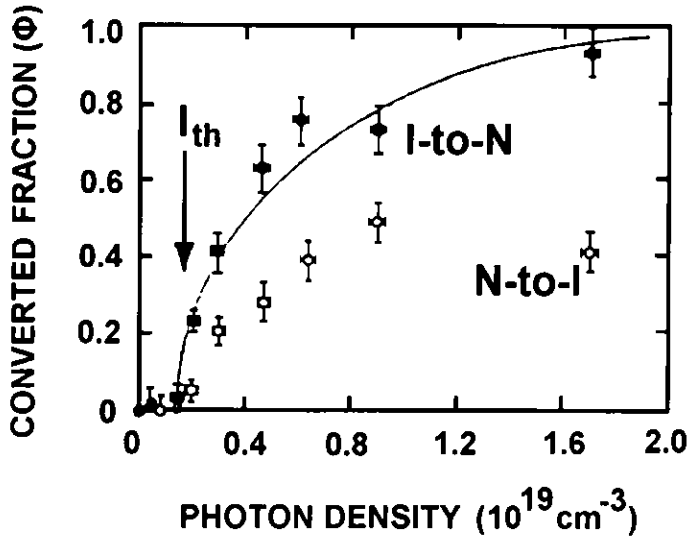

Fig. 2.21: Excitation intensity dependence of the photoconverted fractions (Φ) for I-to-N and N-to-I PIPT. The arrow and $I_{\rm th}$ denote the threshold for excitation. [8]

The photoconverted fraction (Φ) also shows its dependence on the excitation intensity. In Figure 2.21, the excitation-intensity dependencies of Φ for I-to-N and N-to-I are plotted by closed and open circles. The important point in this figure is that Φ increases abruptly if the excitation photon density becomes higher than $I_{\rm th} = 2 \times 10^{18}{\rm cm}^{-3}$. This threshold behavior reveals the highly nonlinear nature of this phase transition.

Not only the excitation intensity but also the excitation energy plays an important role in the PIPT. Recent studies on the PIPT by Suzuki revealed that the direct photoexcitation of the CT absorption band can induce a structural transition from the I-phase to the N one.[9] In Fig. 2.22, we can clearly see that there is a threshold in the intensity for the 1064 nm excitation. The note-worthy character in this figure is the difference between the excitation of 1064 nm and of the 532 nm. The former one is a typical CT excitation, while the later one is due to the intra-molecular excitation of TTF^{+}. It means that a single CT exciton alone can never result in the neutral phase, but only through a nonlinear cooperation between

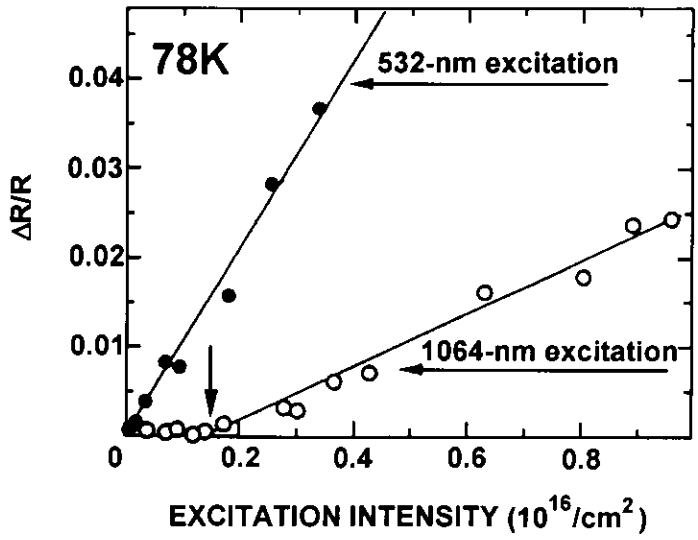

Fig. 2.22: Magnitudes of the reflectance changes at 3.0 eV induced by 1064-nm laser pulse, open circles, and by 532-nm laser pulse, solid circles, as a function of excitation intensity of the laser pulses. [9]

several photo-excited CT excitons, the new phase can be attained. Moreover, the N-phase generation efficiency quite sensitively depends on the way of the excitation. Even if the total absorbed photon energies are same, the difference in the electronic natures of the Franck-Condon state causes the quite different way of relaxation.

Chapter 3

Theory for TTF-CA

To study the physical properties of a molecular crystal, various approaches can be applied with proper approximations. It was clear from early days of quantum mechanics that the systems with 50 $\sim$ 100 molecules are beyond exact quantum mechanical computations in the foreseeable future. We have to resort to some kind of phenomenological theory. As already mentioned, the spectra of CT crystal support the existence of molecules or molecular ions, and hence, the unperturbed molecular states are a suitable starting point for those theories treating only its ground state and low-lying excited states.

In a simple picture, only the highest occupied molecular orbital(HOMO) of the donor is taken into account as well as the lowest unoccupied molecular orbital (LUMO) of the acceptor. The inter-orbital intra-molecular excitations are excluded, since they need much higher energies than the CT excitations do. Thus, in TTF-CA, each TTF(donor) molecule has two electrons to be transferred through the 1-d stack, forming D^{+}, D^{+2} , A^{-} and A^{-2}, while the overall system is neutral. Soos[42] had reviewed the following theoretical model:

$$H = \sum_{n} h_n + \frac{1}{2}{\sum_{n,n'}}' V_{n,n'} + \sum_{n,\sigma} t_{n,n+1}(a^{+}_{n,\sigma}a_{n+1,\sigma} + a^{+}_{n+1,\sigma}a_{n,\sigma}), \qquad (3.1)$$

where h_n and $V_{n,n'}$ respectively denote the on-site Hamiltonians of the n th site, and

the inter-site Hamiltonians of the n th $(n+1)$ th site, while the last term describes the inter-site electron transfer. For the present TTF-CA, h_n can be simplified by

$$h_n = \epsilon_n(a^+_{n,\alpha}a_{n,\alpha} + a^+_{n,\beta}a_{n,\beta}) + U_n a^+_{n,\alpha}a^+_{n,\beta}a_{n,\beta}a_{n,\alpha}, \tag{3.2}$$

in which ϵ_n is the site energy, and U_n is the on-site Coulomb energy.

The inter-site Coulomb interaction $V_{n,n\prime}$ is often called as Madelung energy,

$$V_{n,n\prime} = |M(n,n')|\rho_n\rho_{n'}. \tag{3.3}$$

$M(n,n')$ should be calculated by using the delocalized π-electron charge densities rather than by using the point charge, because the sizes of molecules are comparable to the distance between neighboring molecules. The charge operator ρ_n for an A site is

$$\rho_n = -\sum_\sigma a^+_{n,\sigma}a_{n,\sigma}. \tag{3.4}$$

The net charge at a D site, which is +2 in the vacuum state, is

$$\rho_n = 2 - \sum_\sigma a^+_{n,\sigma}a_{n,\sigma}. \tag{3.5}$$

In many theoretical studies, $V_{n,n\prime}$ is often truncated to the nearest neighbor one($n = n' \pm 1$) V_0, while the missing long-range Coulomb interaction is partially included as a renormalization of V_0.

The inter-site transfer energy $t_{n,n+1}$ is also restricted within the nearest neighbors. Typical values of $t_{n,n+1}$ are in the range of $0.1 \sim 0.5$ eV.

Although the Coulomb interactions between electrons are discussed in detail, the effect of lattice is still not included in the above model. The importance of electron-lattice coupling has been well known in solid state physics for long history. In 1-d systems, any tiny electron-lattice interaction could cause the lattice instability and induce the various deformations in the lattice. One famous example is the Su-Schrieffer-Heeger(SSH) model[44], in which the lattice is dimerized due to weak

electron-lattice interaction. For the present TTF-CA, the remarkable deformation of lattice in N-I phase transition makes the lattice dimerization an important order parameter. Moreover, the nonlinear and threshold behaviors of photoinduced phase transition also give very strong evidence for the important role of the lattice in this system. Therefore, it is reasonable to encompass the lattice potential and electron-lattice interaction into our theoretical model.

3.1 Extended Peierls-Hubbard Model

In order to clarify the unusual experimental phenomena from a unified theoretical point of view, we introduce a modified version of aforementioned model, an extended Peierls-Hubbard model which consists of the following two key points.

(i) One is the Coulomb interactions which nonlinearly depend on the inter-molecular distance. It is well known that the electron-phonon coupling leading to the dimerization may have two origins, the modulation of the inter-molecular(site) Coulomb interaction, and of the inter-molecular(site) electron transfer energy ($\equiv t$). In our model, this coupling is ascribed to the distance dependence of the Coulomb interaction, not due to the modulation of t as in the case of SSH model. Because of the small overlap between the π electron orbitals of donor and acceptor, this t is believed to be so small, that its distance variation can be neglected. In contrast to the SSH model, our model is rather straightforward to make the N-I phase transition to be the first order, even within the mean-field theory with the weak inter-chain interaction.

(ii) The other is the very weak interaction between the neighboring chains. As demonstrated by Fig. 2.7, Fig. 2.8 and Fig. 2.9, the distances between the nearest neighboring TTF and CA molecules along a, b and c axes are about 3.7 Å, 7.6 Å and 14.6 Å, respectively. Although this inter-chain interaction is quite weak, it can bring considerable effects when macroscopic domain structures, different from the

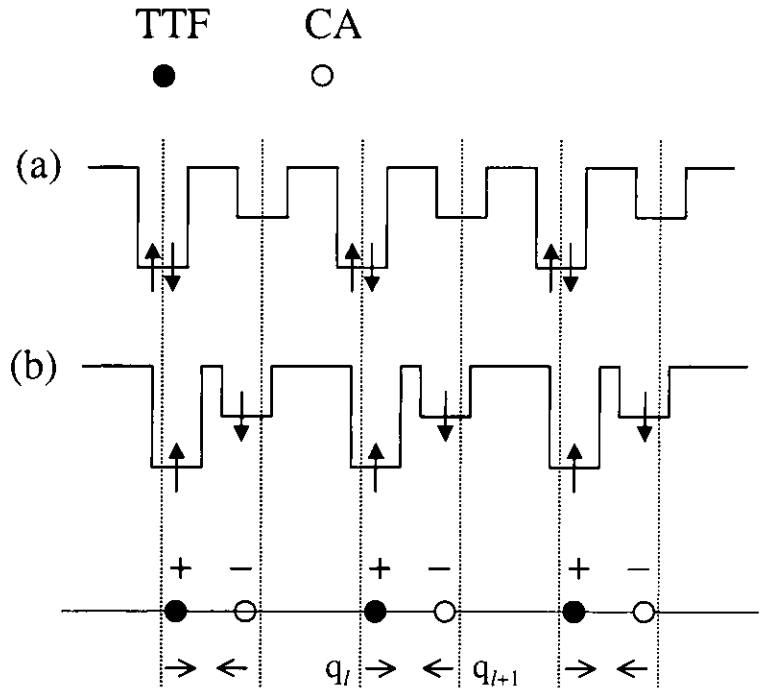

Fig. 3.1: The schematic picture of present theoretical model. (a) Neutral phase. (b) Ionic phase.

ground state, appear in the present three dimensional lattice. Therefore the strong fluctuations in our quasi 1-d system are suppressed by this inter-chain interaction, and it gives a justifiable basis for the mean-field theory.

Let us now proceed to our model Hamiltonian. In our simple-minded picture, the N-phase is such that the HOMO of the donor is filled up with two electrons of opposite spins($\uparrow$ or $\downarrow$), while the LUMO of the acceptor is vacant, as schematically shown in Fig. 3.1(a).

On the other hand, the I-phase is such that the HOMO and the LUMO are equally occupied by the electrons of opposite spins, as shown in Fig. 3.1(b). The energy difference between the doubly ionized donor D^{2+} and the acceptor CA is denoted by Δ, namely the redox energy. Whenever we consider various excitations from the ionic ground state, we focus only on a sample chain, whose total number of

sites is N_t. The donor cations(TTF^{2+}) and the acceptors(CA) sit on the odd(D) and even(A) sites of the chain, alternately. The distance ($\equiv d_{l,l+1}$) between neighboring TTF and CA is given as

$$d_{l,l+1} = d_0(1 + q_{l+1} - q_l) \ , \tag{3.6}$$

where, d_0 is the average inter-molecular distance, and q_l is the relative and dimensionless lattice distortion of l th site. This sample chain is also assumed to be surrounded by neighboring ones, which are always kept in the ionic ground state, no matter whatever various domain structures may occur in this sample chain.

Thus our Hamiltonian($\equiv H$) reads,

$$H = H_{\rm e} + H_{\rm ph} + H_{\rm inter} \ , \tag{3.7}$$

with

$$\begin{aligned} H_{\rm e} \ \equiv \ & -\sum_{l,\sigma} t(C^+_{l,\sigma}C_{l+1,\sigma} + C^+_{l+1,\sigma}C_{l,\sigma}) \\ & + \frac{\Delta}{2}\sum_l (-1)^l n_l + U\sum_l n_{l,\alpha}n_{l,\beta} \\ & - \{ \sum_{l,\rm odd} V_l(q_l, q_{l+1})[2 - n_l]n_{l+1} + \sum_{l,\rm even} V_l(q_l, q_{l+1})[2 - n_{l+1}]n_l \} \ , \\ & n_{l,\sigma} \equiv C^+_{l,\sigma}C_{l,\sigma} \ , \ n_l \equiv \sum_\sigma n_{l,\sigma} \ ; \end{aligned} \tag{3.8}$$

$$H_{\rm ph} \ \equiv \ \sum_l \frac{S_1}{2}(q_l - q_{l+1})^2 + \sum_l \frac{S_2}{4}(q_l - q_{l+1})^4 \ , \tag{3.9}$$

where $H_{\rm e}$, $H_{\rm ph}$ and $H_{\rm inter}$ denote the Hamiltonians of the electron part, the phonon part and the inter-chain one. $C^+_{l,\sigma}(C_{l,\sigma})$ is the creation(annihilation) operator of an electron with spin $\sigma(= \alpha$ or $\beta)$ at l th site. As already mentioned, t is the electron transfer energy and Δ is the site energy difference between TTF^{2+} and CA. U is the on-site Coulomb repulsion. The nearest neighbor Coulomb interaction ($\equiv V_l(q_l, q_{l+1})$) is assumed to depend nonlinearly on the inter-molecular distance as

$$V_l(q_l, q_{l+1}) = V_0 + \beta_1(q_l - q_{l+1}) + \beta_2(q_l - q_{l+1})^2 \ . \tag{3.10}$$

Here V_0 is the constant part, and $\beta_1(\beta_2)$ is its first(second) order expanding coefficient with respect to q_l.

In the phonon part $H_{\rm ph}$ of eq.(3.9), the kinetic energy is neglected because of the adiabatic approximation, and a fourth order potential energy is introduced, as well as the ordinary second order one. The coefficients of these two potentials are denoted by S_1 and S_2, respectively. As will be shown in the Chapter 4, the fourth order potential helps to keep out of unphysically large lattice distortions.

As for the inter-chain coupling term $H_{\rm inter}$, we will neglect it in the study for the ground state properties. This inter-chain interaction is tacitly assumed to have no contribution provided that the ground state is uniform for all over the chains in the crystal, no matter what it will be the dimerized I-phase or the monomeric N one. Its effect also will not be included in the optical absorption spectrum. Only if the macroscopic domain appears in the I-phase, this inter-chain interaction is assumed to bring a considerable energy increase. We will give its practical form later in Chapter 6.

Overall electrical neutrality requires

$$\sum_{l,\rm odd}(2-n_l)=\sum_{l,\rm even}n_l\ , \tag{3.11}$$

and so, $H_{\rm e}$ can be rewritten as

$$\begin{aligned} H_{\rm e} = & -\sum_{l,\sigma} t(C^+_{l,\sigma}C_{l+1,\sigma}+C^+_{l+1,\sigma}C_{l,\sigma}) \\ & +\sum_l \frac{\Delta_{\rm eff}}{2}(-1)^l n_l + U\sum_l n_{l,\alpha}n_{l,\beta} \\ & +\sum_l V_l(q_l,q_{l+1})\ n_l n_{l+1} - \sum_l [V_l(q_l,q_{l+1})+V_{l-1}(q_{l-1},q_l)]n_l\ , \end{aligned} \tag{3.12}$$

where

$$\Delta_{\rm eff}\equiv\Delta-2V_l(q_l,q_{l+1})-2V_{l-1}(q_{l-1},q_l)\ . \tag{3.13}$$

Our model is a simplified version of Sakano and Toyozawa's, in which a point charge model with the long-range Coulomb interaction is adopted.[26]. As mentioned be-

fore, the overlap between the HOMO and the LUMO is tiny, and hence, the transfer energy t also becomes so small, that its distance dependence can be neglected. Therefore, in our model, the electron-phonon coupling entirely comes from the inter-site Coulomb interaction.

3.2 Hartree-Fock Approximation

In order to study the ground state and the single electron excited states, we focus only on the sample chain and neglect the inter-chain interaction. Thus, the remaining part of our Hamiltonian H becomes $(H_{\rm e} + H_{\rm ph})$, and we reduce it to an approximated one $(\equiv H_{\rm HF})$ within the unrestricted Hartree-Fock theory.

$$H_{\rm e} + H_{\rm ph} \longrightarrow H_{\rm HF} \ , \tag{3.14}$$

where

$$\begin{aligned} H_{\rm HF} \ = \ & -\sum_{l,\sigma} t(m_{l,\sigma} + m_{l,\sigma}^{+}) + U\sum_{l,\sigma}(< n_{l,-\sigma} > n_{l,\sigma} - \frac{1}{2} < n_{l,\sigma} >< n_{l,-\sigma} >) \\ & + \sum_{l} V_l(q_l, q_{l+1})(< n_l > n_{l+1} + < n_{l+1} > n_l - < n_l >< n_{l+1} >) \\ & - \sum_{l,\sigma} V_l(q_l, q_{l+1})(< m_{l,\sigma}^{+} > m_{l,\sigma} + < m_{l,\sigma} > m_{l,\sigma}^{+} - < m_{l,\sigma} >< m_{l,\sigma}^{+} >) \\ & - \sum_{l} [V_l(q_l, q_{l+1}) + V_{l-1}(q_{l-1}, q_l)]n_l + \sum_{l} \frac{\Delta_{\rm eff}}{2}(-1)^l n_l \\ & + \sum_{l} \frac{S_1}{2}(q_l - q_{l+1})^2 + \sum_{l} \frac{S_2}{4}(q_l - q_{l+1})^4 \ , \ \ m_{l,\sigma} \equiv C_{l,\sigma}^{+} C_{l+1,\sigma} \ . \end{aligned} \tag{3.15}$$

In this equation, $< \cdots >$ denotes the average over the ground state $(\equiv |g>)$, namely $< \cdots > \equiv < g| \cdots |g >$. We can also define the difference $(\equiv \Delta H)$ between $H_{\rm e} + H_{\rm ph}$ and $H_{\rm HF}$ as,

$$\Delta H = H_{\rm e} + H_{\rm ph} - H_{\rm HF} \ . \tag{3.16}$$

Thus, according to eqs.(3.9), (3.12) and (3.15), ΔH is given by

$$\begin{aligned}\Delta H &= U\sum_l (n_{l,\alpha} - < n_{l,\alpha} >)(n_{l,\beta} - < n_{l,\beta} >) \\ &+ \sum_l V_l(q_l, q_{l+1})(n_l - < n_l >)(n_{l+1} - < n_{l+1} >) \\ &+ \sum_{l,\sigma} V_l(q_l, q_{l+1}) \\ &\times (< m^+_{l,\sigma} > m_{l,\sigma} + < m_{l,\sigma} > m^+_{l,\sigma} - < m_{l,\sigma} >< m^+_{l,\sigma} >) \ . \end{aligned} \tag{3.17}$$

In the ground state, the lattice is assumed to be uniformly dimerized as,

$$q_l = (-1)^l q_0 \ , \tag{3.18}$$

where q_0 is the amplitude of Peierls distortion. Correspondingly, $< n_{l,\sigma} >$ and $< m_{l,\sigma} >$ can also be assumed as

$$\begin{aligned} < n_{l,\sigma} > &= \frac{1}{2} + (-1)^l \delta n_\sigma \ , \\ < m_{l,\sigma} > &= \overline{m}_\sigma + (-1)^l \delta m_\sigma \ , \end{aligned} \tag{3.19}$$

and δn_σ , $\overline{m}_\sigma$ and δm_σ, newly appeared here, should be determined self-consistently later. By using these definitions, the Hamiltonian $H_{\rm HF}$ is now rewritten as,

$$\begin{aligned} H_{\rm HF} = &- \sum_{l,\sigma} [t_{{\rm eff},\sigma} + \alpha_{{\rm eff},\sigma}(-1)^l](m_{l,\sigma} + m^+_{l,\sigma}) \\ &+ \sum_{l,\sigma} \tilde{\Delta}_{{\rm eff},\sigma}(-1)^l n_{l,\sigma} + \tilde{C} \ , \end{aligned} \tag{3.20}$$

where

$$\begin{aligned} t_{{\rm eff},\sigma} &\equiv t + V_{\rm eff}\overline{m}_\sigma + 2\beta_1 q_0 \delta m_\sigma \ , \\ \alpha_{{\rm eff},\sigma} &\equiv 2\beta_1 q_0 \overline{m}_\sigma + V_{\rm eff}\delta m_\sigma \ , \\ \tilde{\Delta}_{{\rm eff},\sigma} &\equiv \frac{\Delta_{\rm eff}}{2} + U\delta n_{-\sigma} - 2V_{\rm eff}\delta n \ , \\ \delta n &\equiv \delta n_\alpha + \delta n_\beta \ , \\ V_{\rm eff} &\equiv V_0 + 4\beta_2 q_0^2 \ , \end{aligned} \tag{3.21}$$

$$\frac{\tilde{C}}{N_t} \equiv \frac{U}{4} - U\delta n_\alpha \delta n_\beta - V_{\rm eff}[1-(\delta n)^2] + V_{\rm eff}\sum_\sigma [(\overline{m}_\sigma)^2 + (\delta m_\sigma)^2] + 4\beta_1 q_0 \sum_\sigma \delta m_\sigma \overline{m}_\sigma + 2S_1 q_0^2 + 4S_2 q_0^4 \ .$$

This compact form of $H_{\rm HF}$ provides us some hints of its numerical solution. The modulation of the effective site-energy $\tilde{\Delta}_{{\rm eff},\sigma}$ indicates the existence of charge density wave(CDW), while the variation of the transfer energy $\alpha_{{\rm eff},\sigma}$ gives arise to bond-order wave. It should be noted that $V_{\rm eff}$ (effective Madelung energy per dimer) is irrelevant to β_1. It can be justified by the fact that the contributions from the linear part of V_l cancel each other, and give no net energy to the ground state, because the lattice displacement $(-1)^l q_0$ is staggered. Although β_1 gives its appearance in $t_{{\rm eff},\sigma}$, its effect is rather limited, because this term originates from the weak exchange between the nearest neighboring molecules. Hence, the second order expanding coefficient β_2 plays a more important role in our theory. Roughly speaking, the energy of the ground state mainly depends on the q_0^2. As for the electrons, the increase of V_l lowers their energies. Consequently, a large lattice distortion may appear if we consider only the second order lattice potential. To suppress this kind of unphysical effect, the fourth order term is necessary.

In the spirit of the adiabatic approximation, each step of the lattice motions is an equilibrium state of the electron subsystem. Therefore, the equilibrium lattice dimerization can be determined by minimizing the total ground state energy as

$$\frac{\partial < H_{\rm HF} >}{\partial q_0} = 0 \ . \tag{3.22}$$

To obtain the one-body eigenvalues and eigenfunctions of $H_{\rm HF}$, we introduce the following new operator ($\equiv a^+_{\lambda,\sigma}$) as

$$a^+_{\lambda,\sigma} = \sum_l f_{\lambda,\sigma}(l) C^+_{l,\sigma} \ . \tag{3.23}$$

so that this unitary transformation can diagonalize $H_{\rm HF}$ as

$$H_{\rm HF} = \sum_{\lambda,\sigma} \epsilon_{\lambda,\sigma} a^{+}_{\lambda,\sigma} a_{\lambda,\sigma} + const. \tag{3.24}$$

Here, $\epsilon_{\lambda,\sigma}$ is the λth eigenvalue of $H_{\rm HF}$ and $f_{\lambda,\sigma}(l)$ is its wavefunction. $\epsilon_{\lambda,\sigma}$ is numbered according to their energies from the lower ones to the upper ones, $\lambda = 1, 2, \cdots, N_t$. Thus, $|g>$ is given as

$$|g> = \prod_{\lambda}^{\rm occ} a^{+}_{\lambda,\alpha} a^{+}_{\lambda,\beta} |0> \quad , \quad |0> \rightarrow \text{true electron vacuum} \ , \tag{3.25}$$

and its energy is

$$E_g = \sum_{\lambda,\sigma}^{\rm occ} \epsilon_{\lambda,\sigma} + const. \tag{3.26}$$

In the numerical calculation, those parameters, δn_σ, $\overline{m}_\sigma$ and δm_σ, should be given as a set of initial values to establish the Hamiltonian $H_{\rm HF}$. According to their definitions in eq. (3.19) and eq.(3.23), they are given in following form

$$\begin{aligned} \delta n_\sigma &= \frac{1}{N_t} \sum_{l,\lambda}^{\rm occ} (-1)^l f^{\star}_{\lambda,\sigma}(l) f_{\lambda,\sigma}(l) \\ \overline{m}_\sigma &= \frac{1}{N_t} \sum_{l,\lambda}^{\rm occ} f^{\star}_{\lambda,\sigma}(l) f_{\lambda,\sigma}(l+1) \\ \delta m_\sigma &= \frac{1}{N_t} \sum_{l,\lambda}^{\rm occ} (-1)^l f^{\star}_{\lambda,\sigma}(l) f_{\lambda,\sigma}(l+1). \end{aligned} \tag{3.27}$$

Then, they can be solved self-consistently by using the iteration method.

3.3 Band Structures

The Hamiltonian can also be solved by the Fourier transformation with a wavevector($\equiv k$) as,

$$C_{k,\sigma} \equiv \frac{1}{\sqrt{N_t}} \sum_{l} \exp(-{\rm i}k \cdot l) C_{l,\sigma} \quad , \quad -\pi \leq k < \pi. \tag{3.28}$$

To illustrate the resultant band structure, we will use this representation. According to eq.(3.20) and eq.(3.28), the $H_{\rm HF}$ in the k-space is

$$\begin{aligned} H_{\rm HF} &= \sum_{k,\sigma} \left[-2t_{\rm eff,\sigma}\cos(k)\right] \left(C^{+}_{k,\sigma}C_{k,\sigma} - C^{+}_{k-\pi,\sigma}C_{k-\pi,\sigma}\right) \\ &+ \sum_{k,\sigma} \left[-2{\rm i}\alpha_{eff,\sigma}\sin(k)\right] \left(C^{+}_{k,\sigma}C_{k-\pi,\sigma} - C^{+}_{k-\pi,\sigma}C_{k,\sigma}\right) \\ &+ \sum_{k,\sigma} \tilde{\Delta}_{eff,\sigma}(C^{+}_{k,\sigma}C_{k-\pi,\sigma} + C^{+}_{k-\pi,\sigma}C_{k,\sigma}) + \tilde{C} \ , \ \frac{-\pi}{2} \leq k < \frac{\pi}{2} \ . \end{aligned} \tag{3.29}$$

By defining the effective band-energy function $\epsilon_{k,\sigma}$, like in a tight-binding model,

$$\epsilon_{k,\sigma} = -2t_{\rm eff,\sigma}\cos(k), \tag{3.30}$$

$H_{\rm HF}$ is given in an easier form for diagonalization,

$$\begin{aligned} H_{\rm HF} &= \sum_{k,\sigma} \epsilon_{k,\sigma}(C^{+}_{k,\sigma}C_{k,\sigma} - C^{+}_{k-\pi,\sigma}C_{k-\pi,\sigma}) \\ &- \sum_{k,\sigma} \sqrt{\left[2\alpha_{eff,\sigma}\sin(k)\right]^2 + \tilde{\Delta}^2_{eff,\sigma}} \\ &\times \left[\exp({\rm i}\Phi_{k,\sigma})C^{+}_{k,\sigma}C_{k-\pi,\sigma} + \exp(-{\rm i}\Phi_{k,\sigma})C^{+}_{k-\pi,\sigma}C_{k,\sigma}\right] + \tilde{C}, \end{aligned} \tag{3.31}$$

where

$$\tan(2\Phi_{k,\sigma}) = \frac{\sqrt{\left[2\alpha_{eff,\sigma}\sin(k)\right]^2 + \tilde{\Delta}^2_{eff,\sigma}}}{\epsilon_{k,\sigma}} \ . \tag{3.32}$$

We introduce the following unitary transformation to diagonalize $H_{\rm HF}$,

$$\begin{aligned} C_{k,\sigma} &= \cos(\theta_{k,\sigma})a_{k,\sigma} + \sin(\theta_{k,\sigma})\exp({\rm i}\Phi_{k,\sigma})b_{k,\sigma} \\ C_{k-\pi,\sigma} &= -\sin(\theta_{k,\sigma})\exp(-{\rm i}\Phi_{k,\sigma})a_{k,\sigma} + \cos(\theta_{k,\sigma})b_{k,\sigma}, \end{aligned} \tag{3.33}$$

in which $a_{k,\sigma}$ and $b_{k,\sigma}$ are newly defined operators, which satisfy the fermion commutation relations,

$$\begin{aligned} \left[a_{k,\sigma}, b^{+}_{k,\sigma}\right] &= 0 \ , \left[b_{k,\sigma}, a^{+}_{k,\sigma}\right] = 0 \ , \\ \left[a_{k,\sigma}, a^{+}_{k,\sigma}\right] &= 1 \ , \left[b_{k,\sigma}, b^{+}_{k,\sigma}\right] = 1 \ . \end{aligned} \tag{3.34}$$

The $H_{\rm HF}$ is then diagonalized as

$$H_{\rm HF} = \sum_{k,\sigma} \sqrt{\epsilon_{k,\sigma}^2 + [2\alpha_{eff,\sigma}\sin(k)]^2 + \tilde{\Delta}_{eff,\sigma}^2}\left(a_{k,\sigma}^{+}a_{k,\sigma} - b_{k,\sigma}^{+}b_{k,\sigma}\right) + \tilde{C}. \qquad (3.35)$$

It is apparent now that $b_{k,\sigma}$ is associated with the occupied states, while $a_{k,\sigma}$ is unoccupied one, if we restrict the system in case of half-filling. After straightforward but lengthy calculation, these self-consistent parameters are obtained in the k-space as,

$$\begin{aligned}
\delta n_\sigma &= \frac{1}{N_t}\sum_k \frac{\tilde{\Delta}_{eff,\sigma}}{\sqrt{\epsilon_{k,\sigma}^2 + [2\alpha_{eff,\sigma}\sin(k)]^2 + \tilde{\Delta}_{eff,\sigma}^2}}, \\
\overline{m}_\sigma &= -\frac{1}{N_t}\sum_k \frac{\epsilon_{k,\sigma}\cos(k)}{\sqrt{\epsilon_{k,\sigma}^2 + [2\alpha_{eff,\sigma}\sin(k)]^2 + \tilde{\Delta}_{eff,\sigma}^2}}, \\
\delta m_\sigma &= -\frac{1}{N_t}\sum_k \frac{2\alpha_{eff,\sigma}[\sin(k)]^2}{\sqrt{\epsilon_{k,\sigma}^2 + [2\alpha_{eff,\sigma}\sin(k)]^2 + \tilde{\Delta}_{eff,\sigma}^2}}.
\end{aligned} \qquad (3.36)$$

3.4 Excited States

Let us now proceed to the excited states. Within the Hartree-Fock approximation, the excited states are such ones that an electron is removed from an occupied level and is put into an unoccupied one. It is denoted by $|n>$, which can be written, according to its definition, as

$$|n> \equiv a_{\lambda_{\rm uocc},\sigma}^{+} a_{\lambda_{\rm occ},\sigma}|g> \quad . \qquad (3.37)$$

It is well known that the Coulomb interaction between the excited electron and the hole left in the valence band, can lower the system energy, and make a bound state called exciton. To include such an exciton effect, we enhance our calculation by the first order perturbation theory as follows. At first, the matrix element($\equiv E_{nn'}^0$) of $H_{\rm HF}$ between the one electron excited states is calculated as

$$E_{nn'}^0 = < n|H_{\rm HF}|n' > \quad . \qquad (3.38)$$

Since $H_{\rm HF}$ had already been diagonalized, it simply gives

$$E^0_{nn'} = \delta_{nn'} < n|H_{\rm HF}|n > \ . \tag{3.39}$$

Then the matrix element($\equiv \Delta E_{nn'}$) of ΔH reads as

$$\Delta E_{nn'} =< n|\Delta H|n' > \ . \tag{3.40}$$

The total energy matrix element ($\equiv E_{nn'}$) is now given by

$$E_{nn'} = E^0_{nn'} + \Delta E_{nn'} \ , \tag{3.41}$$

which has contained the energy correction from the non-Hartree-Fock part. Because there are off-diagonal elements in $E_{nn'}$, the new eigenvalues ($\equiv \tilde{E}_{\tilde{n}}$) and their eigenfunctions ($\equiv |\tilde{n}>$) can be obtained after its numerical diagonalization.

Chapter 4

Ground State Properties

4.1 Parameter Selection

Our way of thinking throughout this work is the phenomenological parameter theory, and we have eight parameters t, Δ, U, V_0, β_1, β_2, S_1 and S_2. These parameters are determined so that, they, only as a set, reproduce main experimental and theoretical results existing already prior to our theory.

According to the *ab-initio* calculation by Katan, we set t at 0.17 eV.[37] There are seven well-known experimental results, listed in Table (4.1). Especially, the transition temperature T_c is an important data which we should address. However, in this work, we will be concerned with only the adiabatic nature at the absolute zero of temperature. Hence, we have to assume some rough relation between the adiabatic nature and T_c. There will be various ways for it. In the present thesis, we simply assume that $k_B T_c$ is roughly equal to the adiabatic barrier ($\equiv E_b$) between the I- and the N-phase at the absolute zero of temperature. This is only an order of magnitude estimation, and it will be explained more in detail later. To reproduce these eight experimental results, we use the following values of theoretical parameters, as listed in Table (4.2).

Parameter	Value	Description
$\rho_{\rm I}$	0.8	Charge-Transfer (I-phase)
$\rho_{\rm N}$	0.3	Charge-Transfer (N-phase)
q_{01}	2.5%	Lattice dimerization (I-phase)
$E_{\rm I1}$	0.6 eV	First CT absorption peak (I-phase)
$E_{\rm I2}$	1.0 eV	Second CT absorption peak (I-phase)
$E_{\rm N}$	0.6 eV	CT absorption peak (N-phase)
$T_{\rm c}$	84 K	N-I phase transition temperature

Table 4.1: Experimental results to be reproduced.

Δ	U	V_0	β_1	β_2	S_1	S_2
2.716	1.528	0.604	1.0	8.54	4.86	3.4×10^3

Table 4.2: List of theoretical parameters. All the values are in the unit of eV.

To avoid the finite size effect, the periodic boundary condition is imposed on the sample chain whose N_t is set at 32.

4.2 Energies and Charge (Spin) Distributions

The calculated adiabatic energies, given by eq.(3.26), are shown in Fig. 4.1(a). Two phases, the I and the N ones, are pseudo-degenerate with each other. The energy minimum of the I-phase is 0.002 eV lower that of the N one, and they are separated by an energy barrier of about 0.0045 eV. Thus the I-phase is the true ground state, while the N-phase is the false one. Furthermore, the lattice of the I-phase is dimerized of about 3% of the lattice constant, while that of the N-phase is not dimerized. As mentioned before, our eight parameters are chosen so that, they, as a set, make the barrier E_b and $k_B T_c$ equal very roughly, because $k_B T_c$ is the energy necessary at each site to excite our system from the ionic state to the neutral one, as the first order phase transition.

In our theory, the inter-site Coulomb interaction is assumed to be the major factor leading to the N-I phase transition. The variation of V_0 could cause a great change in the ground state. Figure 4.1(b) gives us the result with smaller V_0. As shown in this figure, the minimum of the N-phase is 0.0014 eV below that of the I-phase, and hence, the N-phase is, now, the true ground state. In the both cases, the I- and N-phases are all locally stable and are separated by the energy barrier, which is the characteristic of the first order phase transition. When the temperature is lowered down through T_c, the N$\rightarrow$I phase transition occurs. According to the experimental result, this I-phase has 2.5% dimerization of the lattice constant,[11] being close to our theoretical result. From the visible,[1, 2, 3, 6] infrared[2, 4] reflectivity and ESR spectra,[5] this transition is confirmed to be the first order one, as mentioned occasionally.

Figures 4.2(a) and 4.2(b) illustrate the charge and the spin density distributions

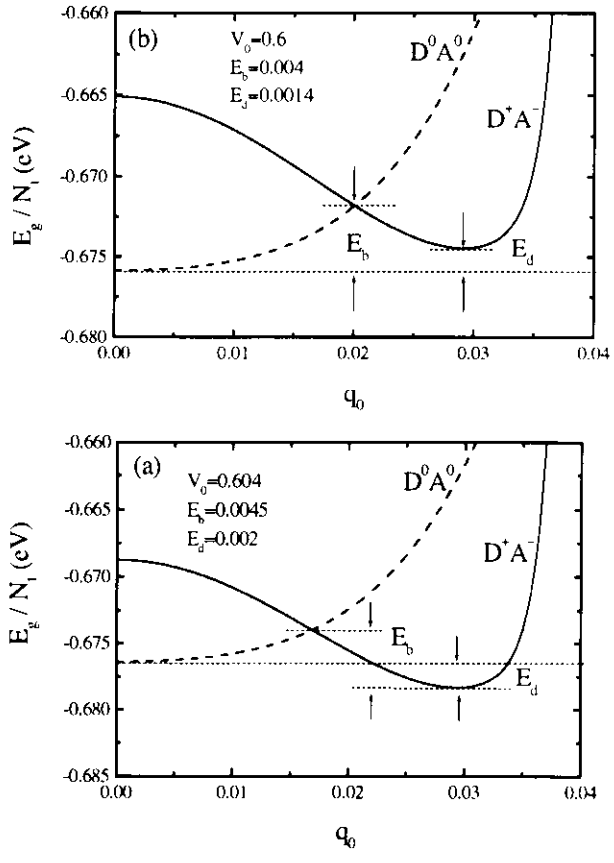

Fig. 4.1: The adiabatic energy (per site) of the ground state. The solid line denotes the ionic phase and the dashed line denotes the neutral one. (a) $V_0 = 0.604$ eV. (b) $V_0 = 0.6$ eV.

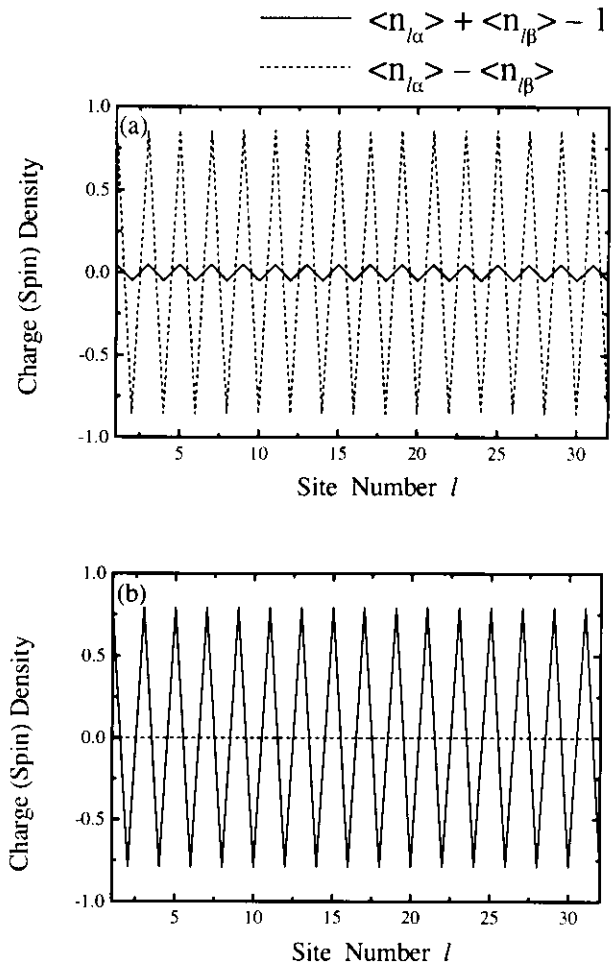

Fig. 4.2: The charge (solid line) and spin(dashed line) density profiles of the ground state. (a) Ionic phase. (b) Neutral phase.

in these I- and N-phases. In the Fig. 4.2(a), the I-phase is characterized by the strong spin density wave (SDW) mixed with the weak charge density wave. The calculated charge transfer is quite large $\rho_{\rm Ic} = 0.95$ and is fractional. As for the N-phase, Figure 4.2(b) demonstrates that there is only the CDW type order. The calculated charge transfer is comparatively small $\rho_{\rm Nc} = 0.2$, but is still significant, due to the finiteness of t in our model. A rough estimation from the data of visible and infrared optical spectra gives $\rho_{\rm N} \approx 0.3$ for the N-phase, and $\rho_{\rm I} \approx 0.8$ for the I one.[6, 4] Thus, our theory can well reproduce these basic experimental data.

Because of the antiferromagnetic character of the I-phase, a staggered magnetic structure and a magnon dispersion relation can be measured by the neutron scattering to determine the natures of this ground state and low energy magnetic excitations therefrom. In the long-wavelength limit, the SDW ground state can be also explored by antiferromagnetic resonance.[43]

4.3 Band Structures

The Figures 4.3(a) and 4.3(b) present the band structures of the aforementioned I- and N-phases. There are four sub-bands in the I-phase, denoted by up(down) arrows to the electron spins, and by D(A) to the donor(acceptor) predominance. Obviously, the two lower sub-bands are occupied, because of the half-filled character of TTF-CA. In contrast, the N-phase has only two sub-bands due to the degeneracy of electrons with opposite spins. According to these band structures, we can describe the one-electron excitations by a schematic picture, which had been originally shown by Sakano and Toyozawa from their long range Coulomb interaction model.[26] For the I-phase, two excitations are available as schematically shown in Fig. 4.4. One is the $(D^{+}A^{-}) \longrightarrow (D^{2+}A^{2-})$ forming a high energy absorption band. The other is $(D^{+}A^{-}) \longrightarrow (D^{0}A^{0})$ forming a low energy absorption band. However, for the N-phase, there is only one excitation $(D^{0}A^{0}) \longrightarrow (D^{+}A^{-})$, due to the double-band structure, as shown in Fig. 4.5.

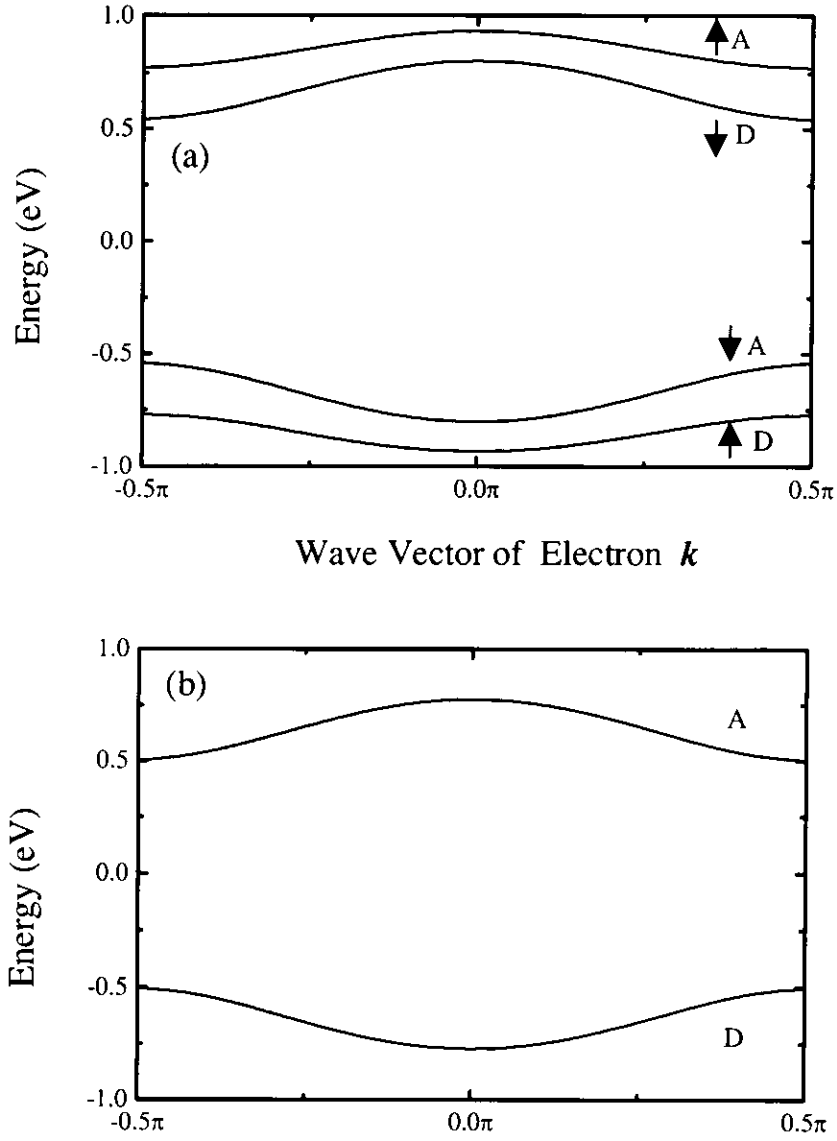

Fig. 4.3: The band structures of TTF-CA. $-\pi/2 \leq \mathbf{k} < \pi/2$. $\uparrow$ and $\downarrow$ correspond to the up and down spins. D and A indicate that the sub-band is predominant by donor or by acceptor. (a) Ionic phase. (b) Neutral phase.

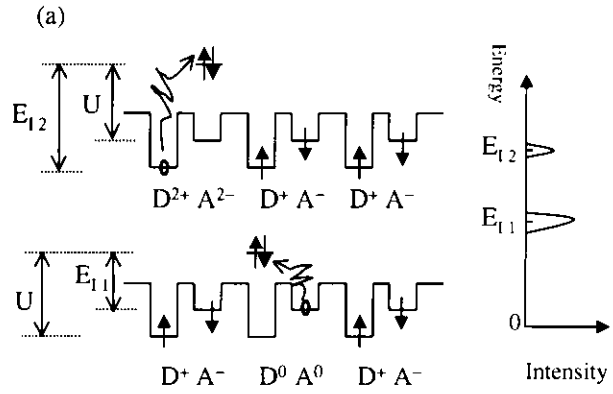

Fig. 4.4: The schematic picture of optical excitations in Ionic phase.

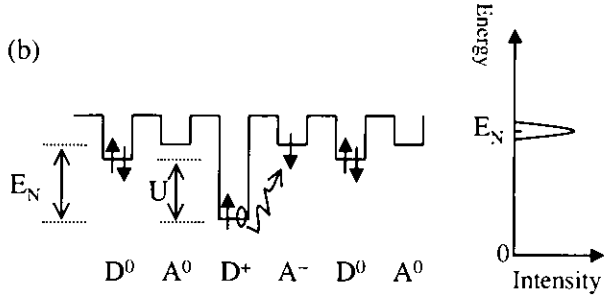

Fig. 4.5: The schematic picture of optical excitation in Neutral phase.

4.4 Magnetic Excitation

As mentioned before, our ionic phase is almost same as the SDW state. Magnetic excitations of this SDW state are described by the well-known Hubbard model,

$$H = -t\sum_{l,\sigma}(C^{+}_{l,\sigma}C_{l\mp1,\sigma} + C^{+}_{l\mp1,\sigma}C_{l,\sigma}) + U\sum_{l} n_{l,\alpha}n_{l,\beta} \ . \tag{4.1}$$

In the case of small t/U limit ($t/U << 1$), the leading term of the expansion with respect to t/U has the form of a uniform Heisenberg model

$$H = J\sum_{l} \vec{S}_l \cdot \vec{S}_{l+1}, \quad J \equiv 2t^2/U \ , \tag{4.2}$$

where J is the exchange integral, and $\vec{S}_l$ is the $\frac{1}{2}$ spin operator at site l. The lowest magnetic excitation of this antiferromagnetic spin system is the gapless spin-wave (or the magnon), as shown in Fig. 4.6(a). If the lattice is dimerized, this uniform exchange integral J undulates with twice the period as

$$J \longrightarrow J_{l,l+1} = J_0 + J_1(-1)^l, \tag{4.3}$$

where J_0 is the constant part, while J_1 is the undulation part due to this dimerization. Such a dimerized spin system is often called Spin-Peierls (SP) system, which has a finite gap in its low energy magnetic excitation, as shown in Fig. 4.6(b).

In our present TTF-CA, the I-phase is expect to be almost same as the SP system, as far as the low energy spin excitation are concerned, because it has the dimerization and each site has only one electron with up(down)spin. The low energy magnetic excitation has also a finite gap, and is located far below the CT excitations as shown in Fig. 4.6(c). However, this is not confirmed by experiments yet.

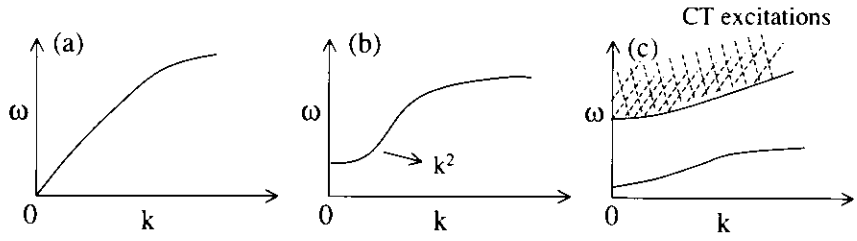

Fig. 4.6: Magnetic excitation spectra in (a) Antiferromagnetic system (b) Spin-Peierls system (c) TTF-CA I-phase. The shadow area of (c) indicates the CT excitations.

Chapter 5

Optical Excited States and Absorption Spectra

5.1 Optical Absorption under Thermal Lattice Fluctuation

In order to calculate the light absorption spectrum, we, now, introduce the following current operator P^m,

$$P^m \equiv \mathrm{i}T' \sum_{l,\sigma} (C^+_{l,\sigma} C_{l+1,\sigma} - C^+_{l+1,\sigma} C_{l,\sigma}) \ , \tag{5.1}$$

where T' is the dipole transition matrix element, which is assumed to be constant. The transition can only occurs from a given site l to its nearest neighbor. The real part of the optical conductivity ($\equiv \sigma(\omega)$) is given as

$$\mathrm{Re}[\sigma(\omega)] = \frac{1}{\omega} \sum_{\tilde{n}} \left| P^m_{\tilde{n},g} \right|^2 \delta(E_{\tilde{n}} - E_g - \hbar\omega) \ , \tag{5.2}$$

where ω is the frequency of incident photon, $P^m_{\tilde{n},g}$ is the matrix element between an excited state $|\tilde{n}>$ and the ground state $|g>$,

$$P^m_{\tilde{n},g} \equiv < \tilde{n}|P^m|g> \ . \tag{5.3}$$

In the finite temperature, the lattice fluctuations are also taken into account in such a way, that, we calculate the ground and the excited states for each randomly generated lattice displacement, one by one. These random configurations are introduced so as to include the thermal lattice fluctuations. The average of $\mathrm{Re}[\sigma(\omega)]$ with respect to the Boltzmann factor ($\equiv W_{\mathrm{B}}(E_g(\{q_l\}))$) is given by

$$\begin{aligned} \mathrm{Re}[\sigma(\omega)] &= \frac{1}{\omega}\int \prod_l \mathrm{d}q_l W_{\mathrm{B}}(E_g(\{q_l\})) \\ &\quad \times \sum_{\tilde{n}} \left|P^m_{\tilde{n},g}\right|^2 \delta(E_{\tilde{n}}(\{q_l\}) - E_g(\{q_l\}) - \hbar\omega) \ , \qquad (5.4) \\ W_{\mathrm{B}}(E_g(\{q_l\})) &= \exp\left(-\frac{E_g(\{q_l\})}{k_{\mathrm{B}}T^\star}\right) \\ &\quad \times \left\{\int \prod_l \mathrm{d}q_l \exp\left(-\frac{E_g(\{q_l\})}{k_{\mathrm{B}}T^\star}\right)\right\}^{-1} \ , \qquad (5.5) \end{aligned}$$

where $E_g(\{q_l\})$ is the energy of the ground state with a random lattice configuration $\{q_l\}$. $T^\star$ is the effective temperature, determined from the real temperature T by the following semi-classical relation,

$$k_{\mathrm{B}}T^\star = \frac{1}{2}\hbar\omega_0 \coth\left(\frac{\hbar\omega_0}{2k_{\mathrm{B}}T}\right) \ . \qquad (5.6)$$

Here, ω_0 is the average frequency of phonons. In our calculation, the classical Monte-Carlo method is adopted with the random lattice configurations created by the Metropolis method.

5.2 Absorption Spectra

Figures 5.1(a) and 5.1(b) exhibit the light absorption spectral shapes without exciton effect and with exciton effect respectively, at the absolute zero of temperature. It reveals that the exciton effect reduces many discrete lines in Fig. 5.1(a) into two main absorption peaks and shifts them to the low energy side. The Figure 5.2 shows the theoretical absorption spectral shape with exciton effect at $T = 45$ K.

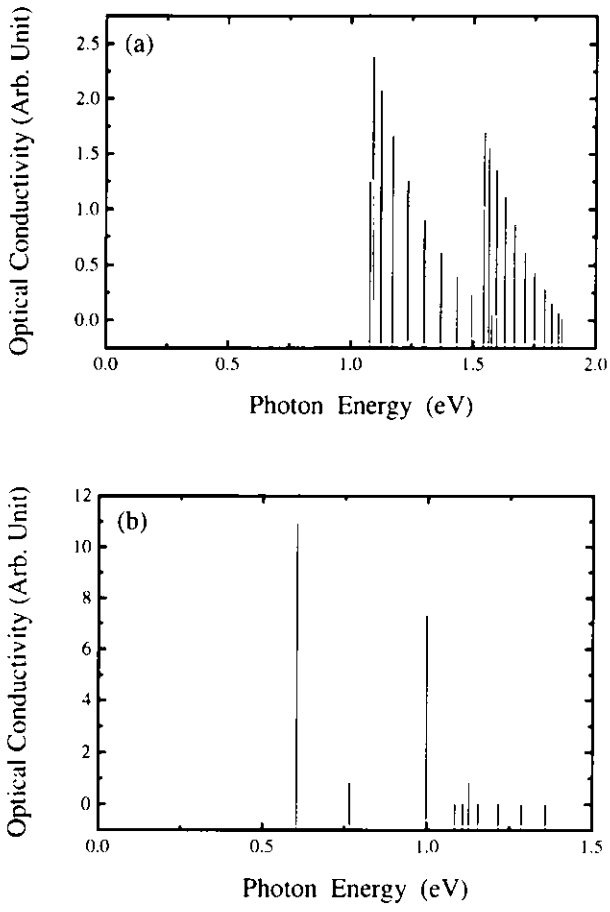

Fig. 5.1: The light absorption spectral shape of the ionic phase at the absolute zero of temperature. (a) Without exciton effect. (b) With exciton effect.

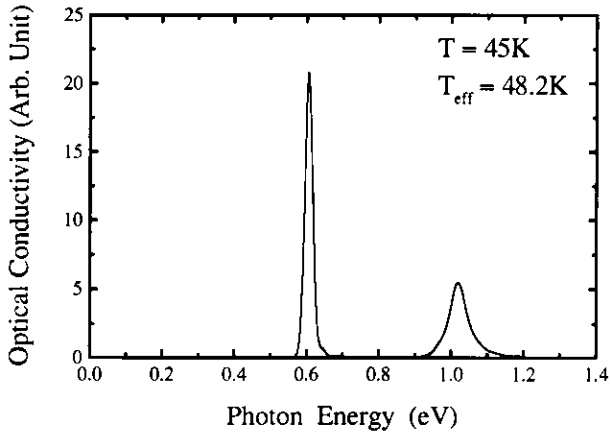

Fig. 5.2: The light absorption spectral shape. T=45 K.

According to the experiment, we adopt $\omega_0 = 0.0036$ eV,[26] and in this case, T^* becomes almost equal to this temperature. In this figure, the spectrum has an intense peak at $E_{I1} = 0.6$ eV and a weak peak at $E_{I2} = 1.0$ eV. It agrees with the experimental results shown in Fig. 2.14, which is obtained by using Kramers-Kronig analysis for the data of optical reflectance.[6].

Our theoretical result well reproduces the positions of these two peaks as well as the relative intensity between them. However, large broadening of the observed two peaks in the experiment, and the large overlap between them, are not reproduced in our present results. They can be ascribed to the other freedoms ignored in our theory. Thus we can conclude that the lowest optical transition in the I-phase is the CT exciton at 0.6 eV, and in the localized picture, it corresponds to the transition from (D^+A^-) to (D^0A^0). As for the N-phase, we can apply the same method developed here, and our theory can well reproduce its peak energy E_N, although we omit our explanation for it.

Chapter 6

Photoinduced Phase Transition

6.1 Photoinduced Phase Transition in TTF-CA

It is well known that an electron in an insulating crystal induces a local lattice distortion around itself when it is excited by a photon. This phenomenon, called lattice relaxation, however has long been tacitly assumed to be a microscopic phenomenon, in which only a few atoms and electrons are involved. Nevertheless, recently discovered unconventionally photoactive solids shake the basis of this picture.[46] In those materials, the relaxation of optical excited states induces various collective motions involving a large number of atoms and electrons. In the final stage of this relaxation, it results in macroscopic excited domain with new structural and electronic orders quite different from the original ones. It is called photoinduced structural phase transition(PISPT).

The present TTF-CA is a good candidate for the studies of this PISPT, since it is close to the N-I transition boundary with the pseudo-degenerate N- and I-phases. In the absolute zero of temperature, the I-phase can have two dimerization patterns $q_l = \pm(-1)^l q_0$, respectively, denoted by IA and IB in Figs. 6.1(a) and 6.1(b). They are perfectly degenerate because of the broken symmetry of spatial inversion along

the chain axis. Moreover the N-phase, shown in Fig. 6.1(c), is just above the I one. As already demonstrated in Sec.4.2, the N-phase is separated from the I one by an energy barrier of about 0.0045 eV per site. The excitations by photons of few eV can supply an enough energy to overcome this barrier and can build a large neutral domain in the true ionic ground state. Of course, such metastable domains will disappear finally within finite lifetime. However, even if they are shortly lived, it is enough for the modern laser spectroscopy techniques to detected those domains.

It is now well established that keeping TTF-CA at the low enough temperature, but shining the strong laser onto it, we can generate a large neutral domain even in the ionic ground state, and this domain is composed of about 200 neutral pairs.[8] A simple scenario for this phenomenon could be given as follows. A single photon can make a single neutral pair, as schematically shown in Fig. 6.1(d), and after that it proliferates through the crystal like a domino game, and finally makes the neutral domain as shown in Fig. 6.1(e). However, this simple scenario is proved wrong experimentally. A single photon can't create such a macroscopic neutral domain, if its energy is just resonated to the CT exciton. Thus, the elementary process of this photoinduced phase transition seems to be highly nonlinear. [9]

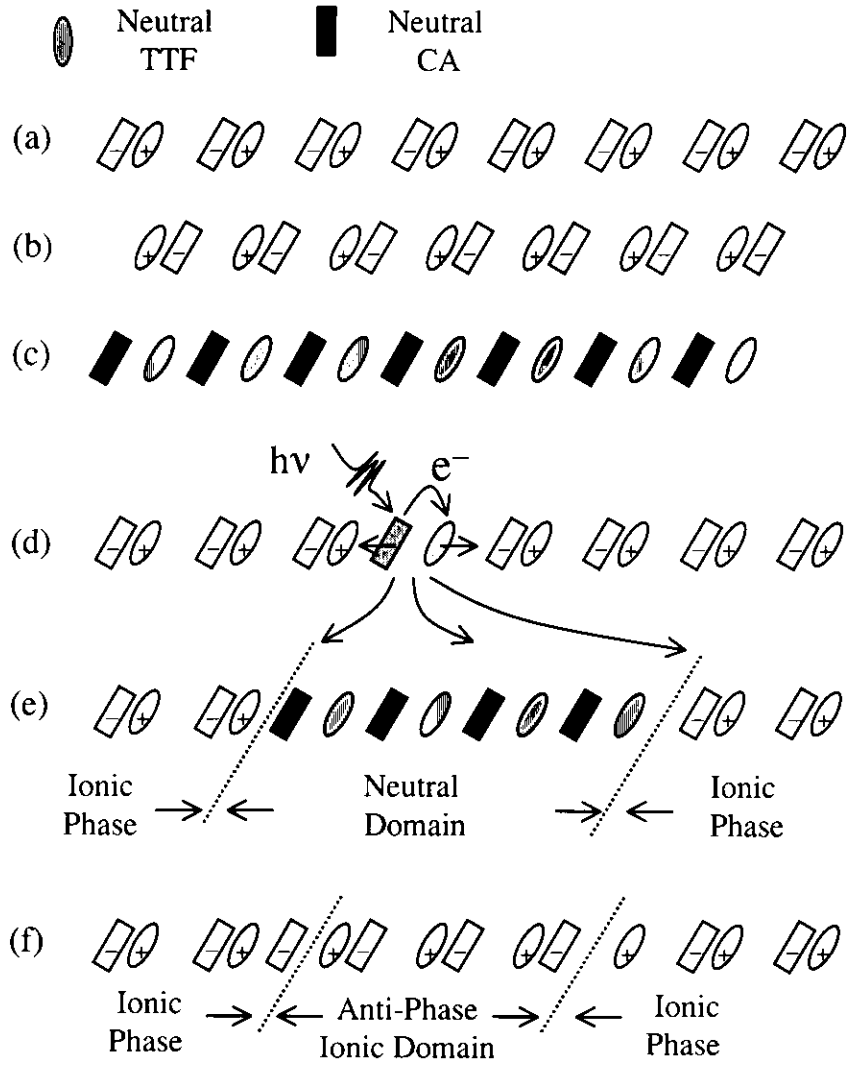

Fig. 6.1: The schematic picture of the photoinduced structural phase transition in TTF-CA. (a) Ionic ground state (IA). (b) Anti-phase ionic ground state (IB). (c) Neutral ground state (N). (d) Charge transfer exciton. (e) Neutral domain. (f) Anti-phase ionic domain.

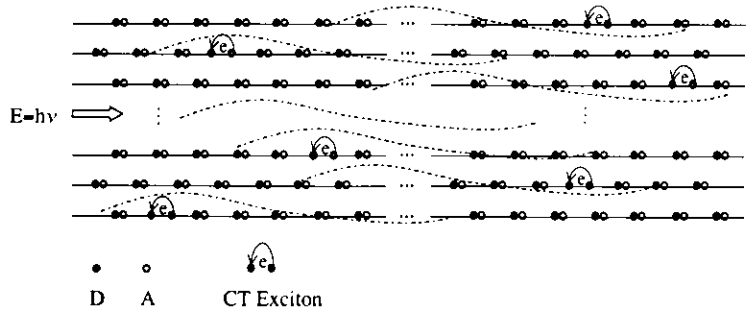

Fig. 6.2: A photon with energy $E = h\nu$ is shone onto the TTF-CA lattice. Its wavelength is much longer than the lattice constant.

6.2 Inter-Chain Interaction

The visible photon has a wavelength of about 1000 times of the lattice constant, and each photon can make a single CT exciton per this length, as schematically shown in Fig. 6.2. Among many excitons thus created in the whole crystal, we will focus only on a single CT exciton and will describe its lattice relaxation.

In order to describe this relaxation, which starts from the Franck-Condon state, and terminates up to the macroscopic neutral domain formation, we introduce the following lattice distortion pattern q_l

$$q_l = (-1)^l q_0 \{1 + \Delta q[\tanh(\theta(|l| - \frac{l_0}{2})) - 1]\} \ . \tag{6.1}$$

Here $(-1)^l q_0$ denotes the Peierls distortion in the ionic ground state, and this q_0 has already been determined by eq.(3.22). The second term in the curly brackets $\{\cdots\}$ denotes the local lattice displacement and Δq is its amplitude. θ corresponds to the spatial extension of this pattern and l_0 is the domain size. The typical domain structures are demonstrated in Fig. 6.3. For $\Delta q < 0.5$, the inner-domain lattice has a reduced dimerization, but is still in the same phase as the outer lattice, and hence corresponds to an ionic domain. In case of second situation $\Delta q = 0.5$, it is obvious that the inner-domain lattice has no dimerization at all. Therefore, it corresponds to a neutral domain. In the third situation $\Delta q > 0.5$, the inner-domain lattice has a reversed dimerization. Thus, it corresponds to an anti-phase ionic domain.

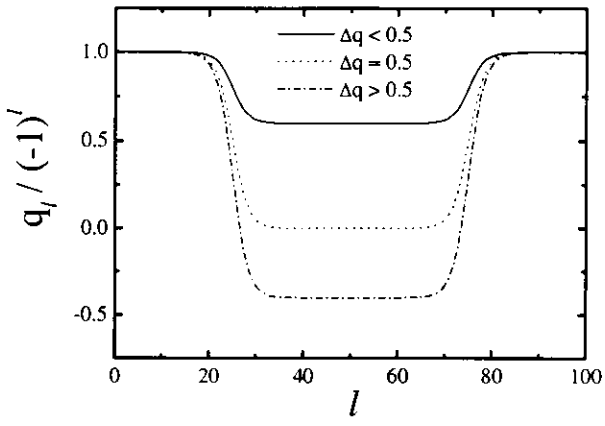

Fig. 6.3: Typical domain structures.

We has hung up the problem for H_{inter} in Sec.3.1, and left the discussion of its expression to this chapter. The inter-chain interaction is tacitly assumed to contribute neither to the uniformly dimerized ground state, nor to the excited states which have only small distortions from the ground state. Only when a new macroscopic domain appears in the dimerized ionic ground state, the inter-chain interaction brings considerable energy increase, even if it is weak and hidden at the Franck-Condon state. For this reason, the practical form of H_{inter} is specified as

$$H_{\text{inter}} = \sum_{l=1}^{N_l} \{K_1[q_l - (-1)^l q_0]^2 + K_2[q_l - (-1)^l q_0]^4 + K_3[q_l - (-1)^l q_0]^6\} . \quad (6.2)$$

Here, q_l is the lattice distortion of the sample chain, while the $(-1)^l q_0$ corresponds to that of the neighboring chains, which are assumed to be always in the ionic ground state and can never be excited.

Such a situation could be justified by the fact that even very strong laser can excite only a small fraction of chains in the TTF-CA crystal. Therefore, an excited chain has much more chances to be surrounded by other nonexcited chains than by other excited ones. In our theory, for simplicity, one of these kind of excited chains is picked up as a sample. We assume that the other part of the crystal are all in the same situation, namely the excited chains are always surrounded by the nonexcited

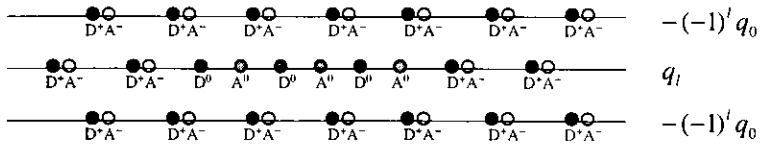

Fig. 6.4: Schematic picture of the chain to be studied and the neighboring ones.

chains. By studying this single sample chain, we deduce the properties of whole crystal from this small part.

As mentioned before, this inter-chain interaction is introduced so as to determine the relative stability between the neutral domain and the anti-phase ionic one. As shown in Fig. 6.4, only relative difference between the present lattice and the starting uniformly dimerized one will be taken into account. It is also assumed to be highly nonlinear with respect to q_l, in the sense that it give no effect when $[q_l - (-1)^l q_0]$ is small. While, when it is large, it will make the system energetically unstable. As one of typical examples to describe such a situation, we take the following coefficients, $K_1 = 0.6949$, $K_2 = -1.415 \times 10^3$, $K_3 = 9.699 \times 10^5$. All the values above are in the unit of eV, and this notation will be used throughout this work, hereafter.

6.3 Nonlinear Lattice Relaxation of CT Exciton

Let us now determine the adiabatic potential energy surface, using these $H_{\rm e}$, $H_{\rm ph}$ and $H_{\rm inter}$. Correspondingly, the self-consistent equations including $< n_{l,\sigma} >$ and $< m_{l,\sigma} >$ are solved for given values of Δq and l_0, while θ is chosen to minimize the lowest excitation energy ($\equiv E_{x1}$).

Since macroscopic neutral domain is expected to appear in the ionic state, the sample chain should be long enough to hold this domain. Experiments have already shown us that about $200 \sim 1000$ ionic neutral pairs could be generated in the ionic phase during this photoinduced N-I phase transition. However, such giant size of chain could make the computation time, which roughly increases as the third power

of total sites, too long to be tolerable. Thus we have to reduce the chain to some reasonable size and assume that for a long chain, only those parts close to neutral domain is important. In the other word, the neutral domain can feel only those ionic pairs which are not so far away, while the other ionic pairs are irrelevant to the neutral domain. We are going to investigate the neutral domain as large as 80 sites within current computation capacity. Based on this consideration, we now set $N_t = 100$.

Because the present lattice is not uniformly dimerized, we can not resort to eq.(3.27) to solve the nonlinear equations for $< n_{l,\sigma} >$ and $< m_{l,\sigma} >$. The parameters related with each l th site should be determined respectively. However, there arise a problem, the self-consistent calculation may not give a unique solution for coupled nonlinear equations. The iteration procedure sometimes meets trouble in convergence and trapped in an oscillatory cycle. A safer and fast-convergence method is needed to replace the straightforward iteration calculation. The direct-minimization algorithm, which had been designed by Fukutome[47], is a good approach to avoid those troubles just mentioned. The detail will be given in the Appendix A.

Figure 6.5 demonstrates the adiabatic energy surface of the ground state. The axis l_0 denotes the domain size, and Δq indicates the amplitude of distortion. All the energies are referenced from the ionic ground states ($l_0 = 0$, $\Delta q = 0$), and this notation is used throughout this thesis hereafter. As already mentioned, the region with $\Delta q < 0.5$ is still the I-phase. Nevertheless, the neutral domain appears and becomes stable in the region $l_0 \geq 40$, just like the nucleation of a gaseous bubble in an overheated liquid. It should be stressed that the threshold size of neutral domain is closely related with the energy difference between I and N ground states. Larger energy difference makes the small neutral domain more unstable and results in much larger domain for the stability. With the current set of parameters, the I ground state is just below the N one so that a stable neutral domain appear at

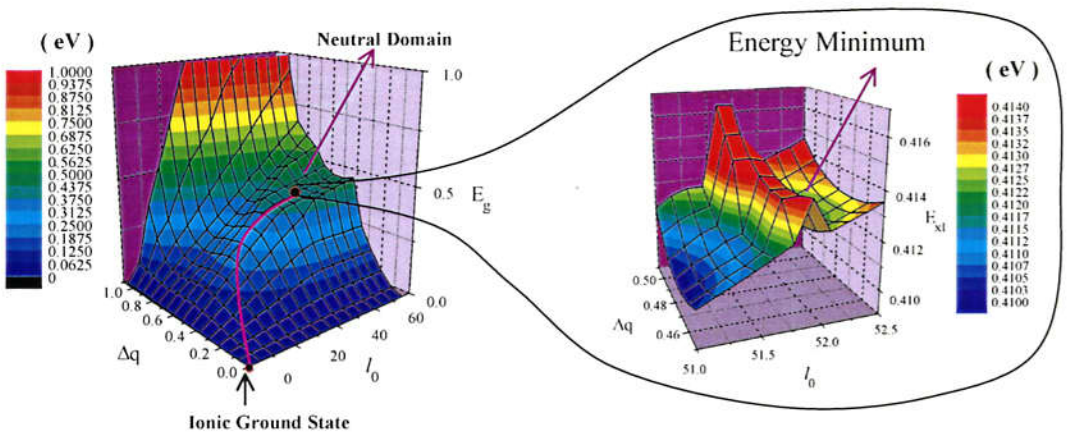

Fig. 6.5: The adiabatic energy surface of the ground state. One of the energy minima is shown in the enlarged inset. The bright purple line indicates the schematic relaxation path from the neutral domain to the true ionic ground state.

40. The region with $\Delta q > 0.5$ and $l_0 > 40$ corresponds to the anti-phase ionic domain. It should be noted that the neutral domain is higher than the ionic ground state, while the anti-phase ionic domain is more above than this neutral domain. The bright purple line in Fig. 6.5 indicates the schematic relaxation path from the neutral domain to the true ionic ground state. There exist various shallow minima on the surface of the ground state in the region of $\Delta \approx 0.5$ and $l_0 > 40$. An example is shown as an enlarged inset of this figure. The presence of these minima makes the decay of neutral domain slow.

Figures 6.6 show the adiabatic energy(E_{x1}) surface of the first excited state, through the front and the back views. The minimum point at $l_0 = 0$ and $\Delta q = 0$ is the Franck-Condon state (the CT exciton). There is another minimum at around $l_0 \approx 40$ and $\Delta q \approx 0.5$. It corresponds to an excited state of the neutral domain, and is separated from the Franck-Condon state by a high barrier. The difference between this excited domain and the ground state one will be explained later.

Figure 6.7 exhibits the adiabatic energy surface along the relaxation path indicated by the bright purple line in Fig. 6.5. The horizontal axis means the number of

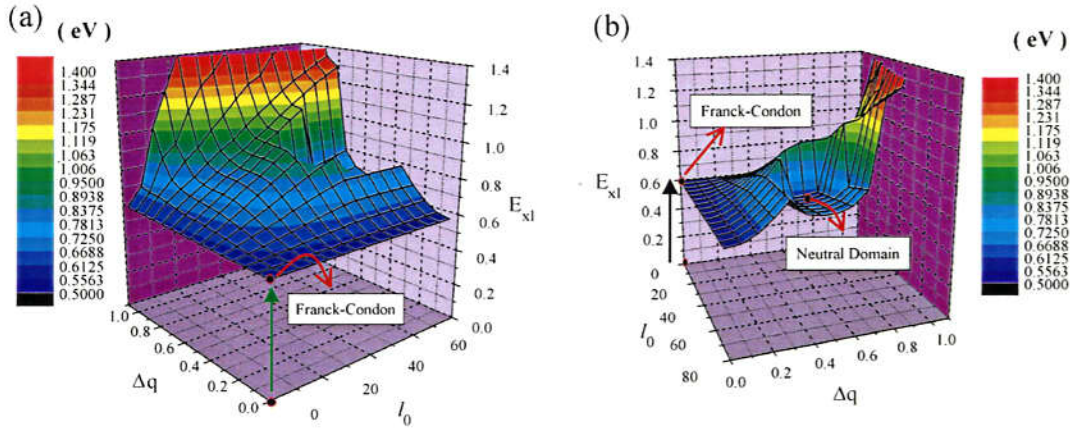

Fig. 6.6: The energy surface of the first excited state. (a) The front view. (b) The back view.

the neutral sites created in the ionic ground state. The energy curve of the first excited state has two local minima, at the region of small $l_0(\approx 0)$ and also at the region of large $l_0(\approx 40)$. As mentioned before, the first one corresponds to the CT exciton, while the second one is the neutral domain, which is a little above the CT exciton. Moreover, these two local minima are separated by a high barrier. This result leads us to a very important conclusion that the lowest state of a single CT exciton can not relax down to the neutral domain straightly, but a large excess energy is necessary so that it can overcome this barrier, as schematically shown by the dash-dot excitation line. If we have such a large excess energy at the Franck-Condon state, this excess energy will be converted into vibronic energies and(or) kinetic energies of excitons, and may induce various nonlinear processes during the relaxation. As for the energy curve of the ground state, roughly speaking, it monotonously increases from the starting ionic ground state to the neutral domain. After the neutral domain has grown up further, the energy gradually increases, due to the energy difference between I-phase and N-phase in Fig. 4.1(a), and also due to the weak inter-chain interaction. Moreover, if we see in detail, there are various shallow minima on the energy curve. One example is shown in the enlarged inset of this figure. These

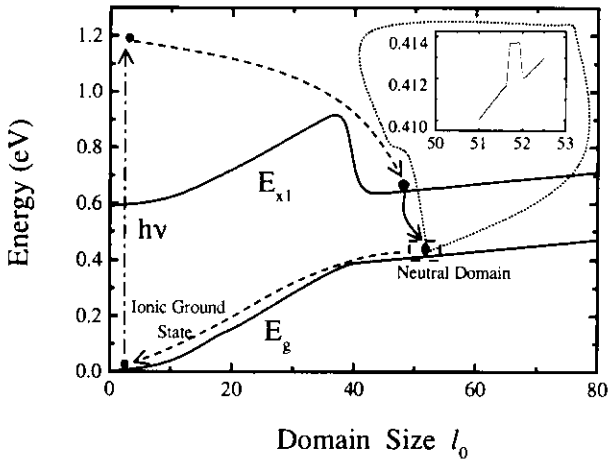

Fig. 6.7: The energy surface along the schematic relaxation path indicated in Fig. 6.5 by the bright purple line. A shallow energy minima in the ground state energy curve is shown in the enlarged inset, as an example.

wrinkles prevent the fast decay of the neutral domain and ensure this domain to be a metastable state.

Figure 6.8 illustrates the adiabatic energies as a function of Δq when the domain size is fixed at $l_0 = 50$. In the energy curve of the first excited state, the state continued from the Franck-Condon state is at $\Delta q = 0$, while the neutral domain is around $\Delta q \approx 0.5$. The anti-phase ionic domain is at $\Delta q \approx 0.7$, and in this state the phase of dimerization is inverted from that of the starting ionic ground state. The region around the local energy minimum of the neutral domain is shown as an enlarged inset. We can see that it is a little below the anti-phase ionic domain, and a low energy barrier separates them. In this situation, even if the anti-phase ionic domain is generated just after the CT excitation by using the excess energy, it can not last long, but soon will relax down to the neutral domain.

We have to point out that the inter-chain interaction is one of the key points. To stress its importance, we also demonstrate the adiabatic energies without the inter-chain interaction in Fig. 6.9. In contrast to Fig. 6.8, the energy of the anti-phase

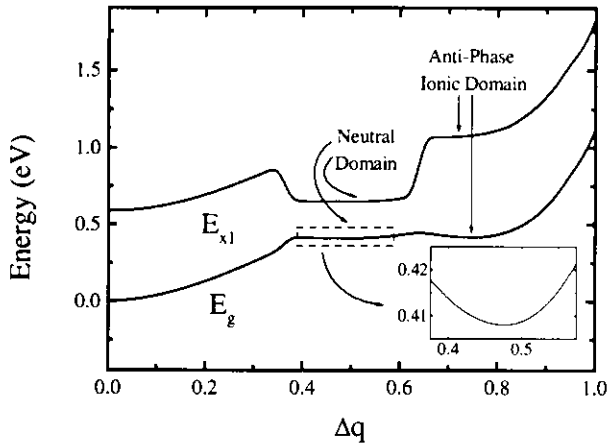

Fig. 6.8: The energies of the ground state and of the first excited state with inter-chain interaction. $l_0 = 50$. The energy minimum of the ground state is shown in the enlarged inset.

ionic domain is much lower than that of the neutral domain in the energy curve of the ground state. In this case, the most stable optical excited state will be this anti-phase ionic domain. However, as mentioned in Sec.2.4, we think that this situation is not realized in the present TTF-CA. By using femto-second photon pulse, it is also recently discovered that there occurs a new transient domain which is clearly different from the neutral one.[8] It is also shown that this new state appears just after the excitation, but soon is converted into the neutral domain. We expect that it is the present anti-phase ionic domain.

Figure 6.10 demonstrates the charge(spin) distribution in the ground and the first excited states of the neutral domain. In the both left and right sides of this chain, the I-phase remains, and is characterized by strong SDW type order mixed with weak CDW type one. While, within the domain, a strong CDW type order appears, and it clearly corresponds to the N-phase. There is almost no SDW type order in this new domain. The boundary between these two phases is called NIDW, as mentioned before, and had been clarified by Nagaosa.[24, 25] The difference between

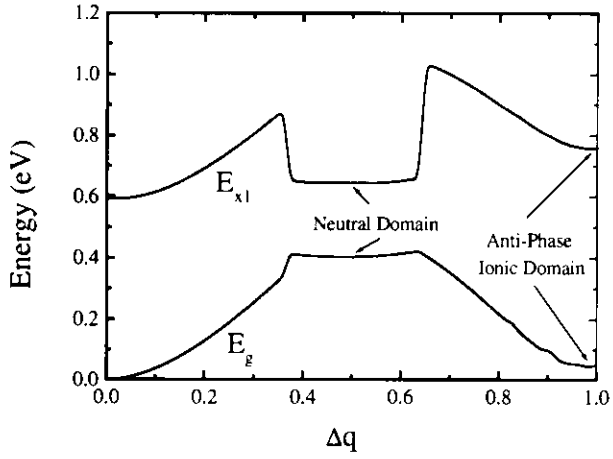

Fig. 6.9: The energies of the ground state and of the first excited state without inter-chain interaction. $l_0 = 50$.

the ground state and the excited one mostly occurs in these NIDW. The sum of charge(spin) over 10 sites around this NIDW unveils that its ground state can carry a unit charge or spin. On the other hand, its first excited state can carry neither charge nor spin.

Let us now see possible decay processes from the excited state to the ground state shown in Fig. 6.10. We have $N_t/2$ electrons for each spin, up and down, and hence, in the ground state, one-electron levels up to $N_t/2$ th from the lowest one, are occupied. While, in the first excited state, this $N_t/2$ th level becomes vacant and the $(N_t/2+1)$ th level is newly occupied. In Fig. 6.11, the wavefunctions of these levels are illustrated for electrons with up spin or down spin. It is apparent that the wavefunctions of these two levels are centered around these NIDW, and have almost no overlap between them. Therefore the radiative or nonradiative transition between these two levels is quite difficult. So that, the first excited state can have fairly long lifetime, as far as, we restrict ourselves within the present mean-field theory.

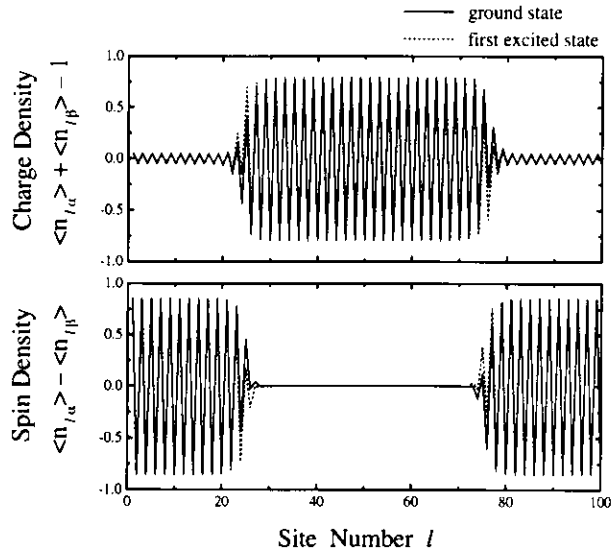

Fig. 6.10: The charge and the spin density profiles of the neutral domain. $l_0 = 50$.

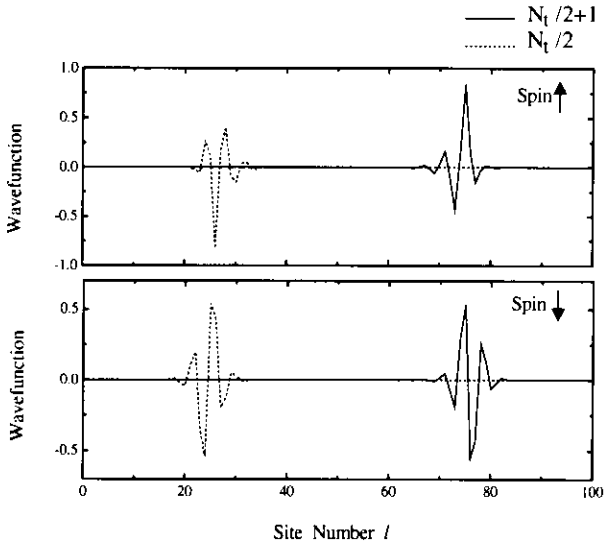

Fig. 6.11: The wavefunctions of the $N_t/2$ th and the $(N_t/2+1)$ th levels.

Chapter 7

Future Prospect

Since a single CT exciton alone can never result in the large neutral domain, the nonlinear cooperation between CT excitons is important to attain the N-phase. According to the discussion in Sec. 6.3, the neutral domains could have long life time due to the barriers which block it back to the initial ground state. Therefore, a early born N-domain can last long enough to 'see' other new-generated ones which are in the same chain, if the photoexcitations are sufficiently strong. Then, these N-domains could attract each other, move closer and finally merge into a large stable neutral domain. This type of aggregation processes will be investigated within our mean-field picture.

It is well known that a pure 1-d systems is unstable against the strong quantum fluctuations. We had argued that our model is effective because these quantum fluctuations are suppressed by the inter-chain interactions. Consequently, a phenomenological expression is introduced for such interactions to clarify the major PIPT properties. However, it is far from satisfaction because the choice of its form is rather arbitrary, and the determination of coefficients is also difficult. The inter-chain interaction is a combination of inter-chain charge transfer and screened Coulomb interactions. We wish to introduce it directly from these factors and de-

termine its strength in a more reliable way.

So far, we have studied the TTF-CA by the adiabatic approximation and mean-field theory on an extended Peierls-Hubbard model. The exclusion of the kinetic energy of lattice makes it difficult for us to investigate any dynamics of the system. According to recently obtained results on the photoinduced NIPT, the early time relaxation contains very interesting physics showing so called initial condition sensitivity. The small difference of initial optical excitation causes remarkable difference of the neutral phase generation efficiency, although the total excitation energy is same. It was also suspected that a transient phase appears only in the early stage of relaxation, in which the anti-phase may be a possible candidate.

These highly nonlinear phenomena require us to survey the time evolution of the lattice relaxation of exciton. Therefore, the fully quantum-mechanical study on both the electron and lattice is extremely important. Because of the limitation in the computation power, the largest numerically solvable systems are composed of only less than 20 lattice sites for a 1-d system. The result of such small size is quite doubtful for any real systems which contain thousands of molecules. Quantum Monte Carlo simulation has been proved to be a powerful method to study the many body problem, but is difficult to treat with low temperature case. Recently, the density matrix renormalization group (DMRG) had also been developed and successfully applied to a variety of low dimensional systems. It is found to be a powerful and robust numerical method for low-lying excited states and correlation functions. Making use of these theoretical methods, we are going to extend our work to the dynamical properties of NIPT and finite temperature behaviors of TTF-CA.

Chapter 8

Conclusion

We have theoretically studied the photoinduced I-N structural phase transition in the organic molecular crystal TTF-CA, from a unified point of view. Using the adiabatic approximation and the mean-field theory, we investigated an extended Peierls-Hubbard model to clarify various features of TTF-CA, ranging from the ground state properties, the absorption spectral shape, to the nonlinear lattice relaxation of the CT exciton. Our model includes strong inter-molecular Coulomb interactions, which depend nonlinearly on the inter-molecular distance. A weak inter-chain interaction was also taken into account to describe the formation of the macroscopic neutral domain in the three dimensional ionic phase. In the ground state, the quasi-I phase is just below the quasi-N one. Both these I- and N-phases are locally stable, and they are separated by a low barrier. In the I-phase, the lattice has 3% dimerization along the stacking axis, while the N one is monomeric and has no dimerization. Based on this mean-field picture, the N-I phase transition in TTF-CA was classified to be the first order. To calculate the optical absorption spectrum, we have developed a classical Monte-Carlo theory to take the thermal lattice fluctuations into account. The exciton effect was also included by using the first order perturbation theory. The resultant spectrum illustrates the peculiar two-headed shape, which agrees with the

experimental one. Thus we could well reproduce the positions of these two peaks as well as the relative intensity between them. It was concluded that the low energy peak corresponds to the transition from (D^+A^-) to (D^0A^0), while the high energy one is due to the transition from (D^+A^-) to $(D^{2+}A^{2-})$.

By studying the nonlinear lattice relaxation processes of the CT exciton, we clarified the adiabatic relaxation path, which starts from its Franck-Condon state and terminates up to the large neutral domain formation in the ionic phase. The ground state energy surface reveals that this neutral domain becomes stable only when its size is large. Moreover, the first excited state of the neutral domain is a little above the Franck-Condon state, and these two states are separated by a high barrier. Therefore the lowest state of a single CT exciton can not relax down to the neutral domain straightly, but a large excess energy is necessary so that it can overcome the barrier. This theoretical result explains the origin of the threshold excitation intensity, below which the macroscopic neutral domain can not be generated by the photons resonated to the CT exciton. It was also discovered that there exist various shallow minima on the energy surface of the ground state. These minima prevent the fast decay of the neutral domain, and let it have a fairly long lifetime. We also investigated the anti-phase ionic domain. This domain is above the neutral one, and a low barrier separates them. Thus, even if the anti-phase ionic domain is generated just after the photoexcitation, it will soon relax down to the neutral one. These findings are consistent to the recently obtained time-resolved experimental results. Furthermore, we illustrated the charge and the spin distributions of the neutral domain. Our results show that the ground state of the NIDW can carry a unit charge and spin, however, its first excited state can carry almost neither of them. The radiative or nonradiative decay of the excited NIDW was found to be quite difficult, so that, the first excited states can have fairly long lifetime, if we restrict ourselves within the mean-field theory.

Acknowledgement

I would like to express my sincere gratitude to my advisor Professor K. Nasu, who has never hesitated to give me his precious suggestions and great encouragements. I was introduced into this new field step-by-step by Prof. Nasu with his knowledge and patience. I am also very grateful to professor H. Zheng, who had been generously offering me so many stimulating discussions during my study in Japan. I would also like to thank Dr. K. Iwano and Dr. N. Tomita for their stimulating discussions on my study. I want to thank Dr. H. Mizouchi for helpful advice on the methods of numerical calculation.

I wish to dedicate this thesis to my parents, who have been the first teachers in my life.

Appendix A

Direct Minimization Algorithm for Unrestricted Hartree-Fock Approximations

The Hartree-Fock (HF) theory is the basic approximation for many fermion systems, and is based on the independent particle picture for motions of these fermions. The present HF theory does not impose any symmetry restrictions and allows broken symmetry orbitals and Slater determinants to appear. It is usually called the unrestricted HF (UHF) theory.

The HF equation in its conventional form is a nonlinear equation. It has been customary solved by the iteration procedure. However, this procedure frequently meets such troubles, that the iteration is trapped in an oscillatory cycle with no exit from it. To avoid this type trouble, Fukutome developed the direct minimization method to secure the convergence and to make the computation fast.[47]

Not loosing generality, a following Hubbard system is taken as an example,

$$H = V + h_{\zeta\eta} a_\zeta^+ a_\eta + \frac{1}{4} [\zeta\eta|\iota\kappa] a_\zeta^+ a_\iota^+ a_\kappa a_\eta, \tag{A.1}$$

where $h_{\zeta\eta}$ is the single particle Hamiltonian, and $[\zeta\eta|\iota\kappa]$ is the antisymmetrized

Coulomb repulsion integral

$$h_{\zeta\eta} = \langle\psi_\zeta|h|\psi_\eta\rangle\,, \tag{A.2}$$

$$[\zeta\eta|\iota\kappa] = \langle\zeta\eta|\iota\kappa\rangle - \langle\zeta\kappa|\iota\eta\rangle\,, \tag{A.3}$$

$$\langle\zeta\eta|\iota\kappa\rangle = \int\int \frac{e^2}{r_{12}}\psi_\zeta^*(1)\psi_\eta(1)\psi_\iota^*(2)\psi_\kappa(2)\mathrm{d}(1)\mathrm{d}(2). \tag{A.4}$$

The dummy index are introduced to sum up repeated indices. We introduce a reference Slater determinant with n electrons occupying the spin orbitals ψ_α, $\alpha = 1, 2, \ldots, n$,

$$|\Psi\rangle = a_1^+ \cdots a_n^+ |0\rangle = \det\left[\psi_\alpha(i)\right], \tag{A.5}$$

In the Slater determinant, the occupied spin orbitals are denoted by the indices $\alpha, \beta, \gamma, \ldots$ and the unoccupied ones by the indices $\mu, \nu, \xi, \ldots$. The indices $\zeta, \eta, \iota, \kappa, \ldots$ denote spin orbitals without specification of occupancy. The Slater determinants with single, double and multiple excitations of electrons are given by

$$|\Psi_{\mu\alpha}\rangle = a_\mu^+ a_\alpha |\Psi\rangle\,, |\Psi_{\mu\nu\alpha\beta}\rangle = a_\mu^+ a_\alpha a_\nu^+ a_\beta |\Psi\rangle\,, \cdots. \tag{A.6}$$

The Slater determinants $|\Psi_{\mu\nu\ldots\alpha\beta\ldots}\rangle$, $\alpha < \beta < \cdots$, and $\mu < \nu < \cdots$ span an orthonormal complete set for the space with n electrons.

Let $\phi_\zeta, \zeta = 1, 2, \ldots, N$ be another set of orthonormal spin orbitals

$$\langle\phi_\zeta|\phi_\eta\rangle = \delta_{\zeta\eta}. \tag{A.7}$$

ϕ_ζ can be expanded by ψ_ζ as

$$\phi_\zeta = \psi_\eta u_{\eta\zeta}\ ,\ u_{\eta\zeta} = \langle\psi_\eta|\phi_\zeta\rangle\,. \tag{A.8}$$

The N dimensional matrix $u = (u_{\zeta\eta})$ is unitary and belongs to the $U(N)$ group. The Slater determinant with n electrons occupying the spin orbitals ϕ_α, $\alpha = 1, 2, \ldots, n$ is therefore given by

$$|\Phi\rangle = (a^+u)_1 \cdots (a^+u)_n |0\rangle \equiv \det\left[\phi_\alpha(i)\right]. \tag{A.9}$$

Now we define a canonical transformation $U(N)$

$$\begin{aligned} U(N)\,|\Psi\rangle &= |\Phi\rangle\,, \\ U(N) &\equiv e^{\Lambda}e^{\Xi}, \end{aligned} \tag{A.10}$$

where

$$\Xi = \xi_{\alpha\beta}a_{\alpha}^{+}a_{\beta} + \overline{\xi}_{\mu\nu}a_{\mu}^{+}a_{\nu}, \quad \xi_{\alpha\beta}^{\star} = -\xi_{\beta\alpha}, \quad \overline{\xi}_{\mu\nu}^{\star} = -\overline{\xi}_{\nu\mu}\ , \tag{A.11}$$

$$\Lambda = \lambda_{\mu\alpha}a_{\mu}^{+}a_{\alpha} - \lambda_{\mu\alpha}^{\star}a_{\alpha}^{+}a_{\mu}\ . \tag{A.12}$$

In this canonical transformation, Λ corresponds to the particle-hole creation process, while Ξ corresponds to the process in which an electron is transferred within the occupied or unoccupied orbitals.

It is not difficult to find

$$\begin{aligned} e^{\Lambda}a_{\alpha}^{+}e^{-\Lambda} &= a_{\beta}^{+}[C(\lambda)]_{\beta\alpha} + a_{\mu}^{+}[S(\lambda)]_{\mu\alpha}, \\ e^{\Lambda}a_{\mu}^{+}e^{-\Lambda} &= a_{\nu}^{+}[\tilde{C}(\lambda)]_{\nu\mu} - a_{\alpha}^{+}[S^{+}(\lambda)]_{\alpha\mu}. \end{aligned} \tag{A.13}$$

This transformation is equivalent to the following transformation of the orbitals ψ_{ζ} to mix the occupied and unoccupied ones:

$$\begin{aligned} \phi_{\alpha} &= \psi_{\beta}[C(\lambda)]_{\beta\alpha} + \psi_{\mu}[S(\lambda)]_{\mu\alpha}\ , \\ \phi_{\mu} &= \psi_{\nu}[\tilde{C}(\lambda)]_{\nu\mu} - \psi_{\alpha}[S^{+}(\lambda)]_{\alpha\mu}\ . \end{aligned} \tag{A.14}$$

The $S(\lambda)$, $C(\lambda)$, and $\tilde{C}(\lambda)$ are the $(N-n)\times n$, $n\times n$, and $(N-n)\times(N-n)$ matrices defined from the $(N-n)\times n$ matrix $\lambda = (\lambda_{\mu\alpha})$ by

$$\begin{aligned} S(\lambda) &= \sum_{k=0}^{\infty}\frac{(-1)^{k}}{(2k+1)!}\lambda(\lambda^{+}\lambda)^{k}, \\ C(\lambda) &= 1_{n} + \sum_{k=1}^{\infty}\frac{(-1)^{k}}{(2k)!}(\lambda^{+}\lambda)^{k}, \\ \tilde{C}(\lambda) &= 1_{N-n} + \sum_{k=1}^{\infty}\frac{(-1)^{k}}{(2k)!}(\lambda\lambda^{+})^{k}\ . \end{aligned} \tag{A.15}$$

After lengthy calculation, the HF energy function is given by

$$E_H(\Phi) = \langle\Phi|H|\Phi\rangle = V + h_{\zeta\eta}Q_{\eta\zeta} + \frac{1}{2}[\zeta\eta|\iota\kappa]Q_{\eta\zeta}Q_{\kappa\iota}, \tag{A.16}$$

$$Q = \frac{1}{2}\begin{bmatrix} 1_n + C(2\lambda), & S^+(2\lambda) \\ S(2\lambda), & 1_{N-n} - \tilde{C}(2\lambda) \end{bmatrix} . \tag{A.17}$$

Equation (A.16) can be rewritten as

$$\begin{aligned} E_H(\Phi) &= E_H(\Psi) + F_{\zeta\eta}(Q-P)_{\eta\zeta} \\ &\quad + \frac{1}{2}[\zeta\eta|\iota\kappa](Q-P)_{\eta\zeta}(Q-P)_{\kappa\iota} , \\ F_{\zeta\eta} &= h_{\zeta\eta} + [\zeta\eta|\alpha\alpha] , \\ E_H(\Psi) &= V + h_{\alpha\alpha} + \frac{1}{2}[\alpha\alpha|\beta\beta], \end{aligned} \tag{A.18}$$

where $P = 1_n$ is the density matrix composed of the occupied orbitals ψ_α, $F_{\zeta\eta}$ and $E_H(\Psi)$ are the Fock operator and the HF energy function for the Slater determinant $|\Psi>$.

We can introduce a new representation of orbitals to diagonalize the matrix λ. We define

$$\begin{aligned} \phi_A &= \phi_\alpha v_{\alpha A} \ , \ \tilde{\phi}_A = \phi_\mu \tilde{v}_{\mu A} \ , \\ \psi_A &= \psi_\alpha v_{\alpha A} \ , \ \tilde{\psi}_A = \psi_\mu \tilde{v}_{\mu A} \ . \end{aligned} \tag{A.19}$$

The orbitals defined in eq. (A.19) satisfy

$$\begin{aligned} \langle\psi_A|\psi_B\rangle &= \langle\tilde{\psi}_A|\tilde{\psi}_B\rangle = \delta_{AB}, \quad \langle\psi_A|\tilde{\psi}_B\rangle = 0, \\ \langle\phi_A|\phi_B\rangle &= \langle\tilde{\phi}_A|\tilde{\phi}_B\rangle = \delta_{AB}, \quad \langle\phi_A|\tilde{\phi}_B\rangle = 0 \ . \end{aligned} \tag{A.20}$$

We obtain, from eqs. (A.14) and (A.20),

$$\begin{aligned} \phi_A &= \psi_A \cos\lambda_A + \tilde{\psi}_A \sin\lambda_A, \\ \tilde{\phi_A} &= \tilde{\psi}_A \cos\lambda_A - \psi_A \sin\lambda_A, \quad A = 1, \ldots, k \\ \phi_A &= \psi_A \quad \text{for } n > M \quad \text{and} \quad n \geq A > N = n, \qquad \text{(A.21)} \\ \tilde{\phi}_A &= \tilde{\psi}_A \quad \text{for } n < M \quad \text{and} \quad N - n \geq A > n. \qquad \text{(A.22)} \end{aligned}$$

The density matrix (A.17) in this representation becomes

$$(Q-P)_{\zeta\eta} = \sum_{A=1}^{k} \frac{1}{2} \begin{bmatrix} v, & 0 \\ 0, & \tilde{v} \end{bmatrix}_{\zeta A} \begin{bmatrix} \cos 2\lambda_A - 1, & \sin 2\lambda_A \\ \sin 2\lambda_A, & 1-\cos 2\lambda_A \end{bmatrix} \times \begin{bmatrix} v^+, & 0 \\ 0, & \tilde{v}^+ \end{bmatrix}_{A\eta} . \tag{A.23}$$

Substitution of eq. (A.23) into eq. (A.18) yields

$$\begin{aligned} E_H(\Phi) &= E_H(\Psi) + \frac{1}{2}\sum_{A=1}^{k}\{k_A(1-\cos 2\lambda_A) + 1_A \sin 2\lambda_A\} \\ &\quad + \frac{1}{8}\sum_{A,B=1}^{k}\{[\tilde{A}\tilde{A} - AA|\tilde{B}\tilde{B} - BB](1-\cos 2\lambda_A)(1-\cos 2\lambda_B) \\ &\quad + [A\tilde{A} + \tilde{A}A|B\tilde{B} + \tilde{B}B]\sin 2\lambda_A \sin 2\lambda_B \qquad \text{(A.24)} \\ &\quad + 2[A\tilde{A} + \tilde{A}A|\tilde{B}\tilde{B} - BB]\sin 2\lambda_A(1-\cos 2\lambda_B)\}, \\ k_A &= F_{\tilde{A}\tilde{A}} - F_{AA} , \qquad 1_A = F_{\tilde{A}A} + F_{A\tilde{A}}, \qquad \text{(A.25)} \end{aligned}$$

where the indices A and $\tilde{A}$ represent the orbitals ψ_A and $\tilde{\psi}_A$, respectively.

Now let Ψ and Φ be the Slater determinants in the iteration cycles i and $i+1$. Their orbitals are related by a matrix $\lambda^{(i)} = (\lambda^{(i)}_{\mu\alpha})$ in the manner of eq. (A.14). Since the off-diagonal matrix elements $F_{\mu\alpha}$ of the Fock operator must satisfy $F_{\mu\alpha} = 0$ in the SCF limit, $v^{(i)}$ and $\tilde{v}^{(i)}$ is determined so as to diagonalize the Fock operator $F^{(i)}_{\mu\alpha}$ at the iteration cycle i,

$$F^{(i)}_{\mu\alpha} = \sum_{A=1}^{k} \tilde{v}^{(i)}_{\mu A} F^{(i)}_{A} v^{(i)\star}_{\alpha A} . \tag{A.26}$$

Then, in the MO basis of the orbitals defined in eq. (A.19),

$$\psi^{(i)}_A = \psi^{(i)}_\alpha v^{(i)}_{\alpha A}, \quad \tilde{\psi}^{(i)}_A = \psi^{(i)}_\mu \tilde{v}^{(i)}_{\mu A}, \tag{A.27}$$

the number of nonzero matrix elements of the off-diagonal Fock operator is minimized. In order to optimize convergence efficiency, the Fletcher-Reeves (1964) conjugate gradient technique is applied in the determination of $v^{(i)}$ and $\tilde{v}^{(i)}$. Instead of

eq. (A.26), they are determined to diagonalize the matrix $R^{(i)} = (R^{(i)}_{\mu\alpha})$ defined by

$$\begin{aligned} R^{(i)}_{\mu\alpha} &= F^{(i)}_{\mu\alpha} + \beta^{(i-1)} R^{(i-1)}_{\mu\alpha}, \quad R^{(1)}_{\mu\alpha} = F^{(1)}_{\mu\alpha} \ , \\ \beta^{(i-1)} &= \sum_{\mu\alpha} \left| F^{(i)}_{\mu\alpha} \right|^2 / \sum_{\mu\alpha} \left| F^{(i-1)}_{\mu\alpha} \right|^2 \ , \\ R^{(i)}_{\mu\alpha} &= \sum_{A=1}^{k} \tilde{v}^{(i)}_{\mu A} R^{(i)}_{A} v^{(i)\star}_{\alpha A} \ . \end{aligned} \tag{A.28}$$

Next, λ_A is determined to minimize the quadratic approximation of eq. (A.24) at iteration cycle i,

$$\begin{aligned} \delta E^{(i)}_{H} &= \sum_{A=1}^{k} \left(1^{(i)}_{A} \lambda_A + \frac{1}{2} k^{(i)}_{A} \lambda^2_A \right) \\ &\quad + \frac{1}{2} \sum_{A,B=1}^{k} \left[A\tilde{A} + \tilde{A}A | B\tilde{B} + \tilde{B}B \right]^{(i)} \lambda_A \lambda_B \ , \end{aligned} \tag{A.29}$$

and put

$$\lambda^{(i)}_{A} = l \lambda_A \ . \tag{A.30}$$

By substituting eq. (A.30) into eq. (A.24), the energy becomes a function of l. We determine l so as to minimize the energy using the power series expansion in l up to the fourth or sixth order.

To sum up, the direct minimization procedure consists of the following iteration cycle:

1. calculate $F_{\mu\alpha}$;
2. determine v, $\tilde{v}$ by eq. (A.28);
3. calculate K_A,1_A, *etc.*, using the orbital (A.27);
4. determine λ_A to minimize (A.29);
5. calculate new trial orbitals by eq. (A.24) with $\lambda^{(i)}_{A}$;

6. check the convergence condition. If the desired accuracy is reached, stop the iteration. Otherwise, go to step 1.

Thus, the iteration completes.

Bibliography

[1] J. B. Torrance, J. E. Vazquez, J. J. Mayerle and V. Y. Lee: Phys. Rev B **46** (1981) 253.

[2] J. B. Torrance, A. Girlando, J. J. Mayerle, J. I. Crowley, V. Y. Lee, P. Batail and S. J. LaPlaca: Phys. Rev. Lett. **47** (1981) 1747.

[3] Y. Tokura, T. Koda, T. Mitani and G. Saito: Solid State Commun. **43** (1982) 757.

[4] A. Girlando, F. Marzola, C. Pecile and J. B. Torrance: J. Chem. Phys. **79** (1983) 1075.

[5] T. Mitani, G. Saito, Y. Tokura and T. Koda: Phys. Rev. Lett. **53** (1984) 842.

[6] C. S. Jacobsen and J. B. Torrance: J. Chem. Phys. **78** (1983) 112.

[7] S. Koshihara, Y. Tokura, T. Mitani, G. Saito and T. Koda: Phys. Rev. B **42** (1990) 6853.

[8] S. Koshihara, Y. Takahashi, H. Sakai, Y. Tokura and T. Luty: J. Phys. Chem. B **103** (1999) 2592.

[9] T. Suzuki, T. Sakamaki, K. Tanimura, S. Koshihara and Y. Tokura: Phy. Rev. B **60** (1999) 6191.

[10] J. J. Mayerle, J. B. Torrance and J. I. Crowley: Acta Cryst. B **35** (1979) 2988.

[11] M. Le Cointe, M. H. Lemée-Cailleau, H. Cailleau, B. Toudic, L. Toupet, G. Heger, F. Moussa, P. Schweiss, K. H. Kraft and N. Karl: Phys. Rev. B **51** (1995) 3374.

[12] M. Le Cointe, J. Gallier, H. Cailleau, M. Gourdji, A. Péneau and L. Guibé: Solid State Commun. **94** (1995) 455.

[13] Y. Kaneko, S. Tanuma, Y. Tokura, T. Koda, T.Mitani, and G. Saito: Phys. Rev. B **35** (1987) 8024.

[14] K. Takaoka, Y. Kaneko, H. Okamoto, Y. Tokura, T. Koda, T. Mitani and G. Saito: Phys. Rev. B **36** (1987) 3884.

[15] J. B. Torrance: Mol. Cryst. Liq. Cryst. **126** (1985) 55.

[16] Y. Tokura, Y. Kaneko, H. Okamoto, S. Tanuma, T. Koda, T. Mitani and G. Saito: Mol. Cryst. Liq. Cryst. **125** (1985) 71.

[17] Y. Tokura, S. Koshihara, Y. Iwasa, H. Okamoto, T. Komatsu, T. Koda, N. Iwasawa and G. Saito: Phys. Rev. Lett. **21** (1989) 2405.

[18] H. Okamoto, T. Mitani, Y. Tokura, S. Koshihara T. Komatsu, Y. Iwasa and T. Koda: Phys. Rev. B **43** (1991) 8224.

[19] M. H. Lemée-Cailleau, M. Le Conite, H. Cailleau, T. Luty, F. Moussa, J. Roos, D. Brinkmann, B. Toudic, C. Ayache and N. Karl: Phys. Rev. Lett. **79** (1997) 1690.

[20] J. Gallier, B. Toudic, Y. Delugeard, H. Cailleau, M. Gourdji, A. Péneau, and L. Guibé: Phys. Rev. B **47** (1993) 11688.

[21] Z. G. Soos and S. Mazumdar: Phys. Rev. B **18** (1978) 1991.

[22] N. Nagaosa and J. Takimoto: J. Phys. Soc. Jpn. **55** (1986) 2735.

[23] N. Nagaosa and J. Takimoto: J. Phys. Soc. Jpn. **55** (1986) 2745.

[24] N. Nagaosa: J. Phys. Soc. Jpn. **55** (1986) 2754.

[25] N. Nagaosa: Solid State Commun. **57** (1986) 179.

[26] T. Iizuka-Sakano and Y. Toyozawa: J. Phys. Soc. Jpn. **65** (1996) 671.

[27] Z. G. Soos, S. Kuwajima and R. H. Harding: J. Chem. Phys. **85** (1986) 601.

[28] Z. G. Soos and S. Kuwajima: Chem. Phys. Lett. **122** (1985) 315.

[29] A. Painelli and A. Girlando: J. Chem. Phys. **87** (1987) 1705.

[30] A. Painelli and A. Girlando: Phys. Rev. B **37** (1988) 5748.

[31] A. Girlando and A. Painelli: Phys. Rev. B **34** (1986) 2131.

[32] M. Avignon, C. A. Balseiro, C. R. Proetto and B. Alascio: Phys. Rev. B**33** (1986) 205.

[33] B. Horovitz and J. Sólyom: Phys. Rev. B **35** (1987) 7081.

[34] T. Luty: J. Chem. Phys. **87** (1987) 3137.

[35] T. Luty and B. Kuchta: Phys. Rev. B **35** (1987) 8542.

[36] T. Luty: J. Phys. Soc. Jpn. **61** (1992) 3636.

[37] C. Katan, C. Koenig and P. E. Blöchl: Solid State Commun. **102** (1997) 589.

[38] B. Horovitz and B. Schaub: Phys. Rev. Lett. **50** (1983) 1942.

[39] J. Hubbard and J. B. Torrance: Phys. Rev. Lett. **47** (1981) 1750.

[40] R. Bruinsma, P. Bak and J. B. Torrance: Phys. Rev. B **27** (1983) 456.

[41] H. M. McConnell, B. M. Hoffman, and R. M. Metzger, Proc. Natl. Acad. Sci., U.S.A. **53** (1965) 46.

[42] Z. G. Soos: Ann. Rev. Phys. Chem. **25** (1974) 121.

[43] G. Grüner: Rev. Mod. Phys. **66** (1994) 1.

[44] W. P. Su, J. R. Schrieffer and A. J. Heeger: Phys. Rev. B **22** (1980) 2099.

[45] M. Hase, I. Terasaki, K. Uchinokura: Phys. Rev. Lett. **70** (1993) 3651.

[46] K. Nasu: *Relaxations of Excited States and Photo-Induced Structural Phase Transitions* (Springer, Berlin, 1997).

[47] H. Fukutome: Int. J. Quantum Chem. **5** (1981) 955.